

AD-A046 840

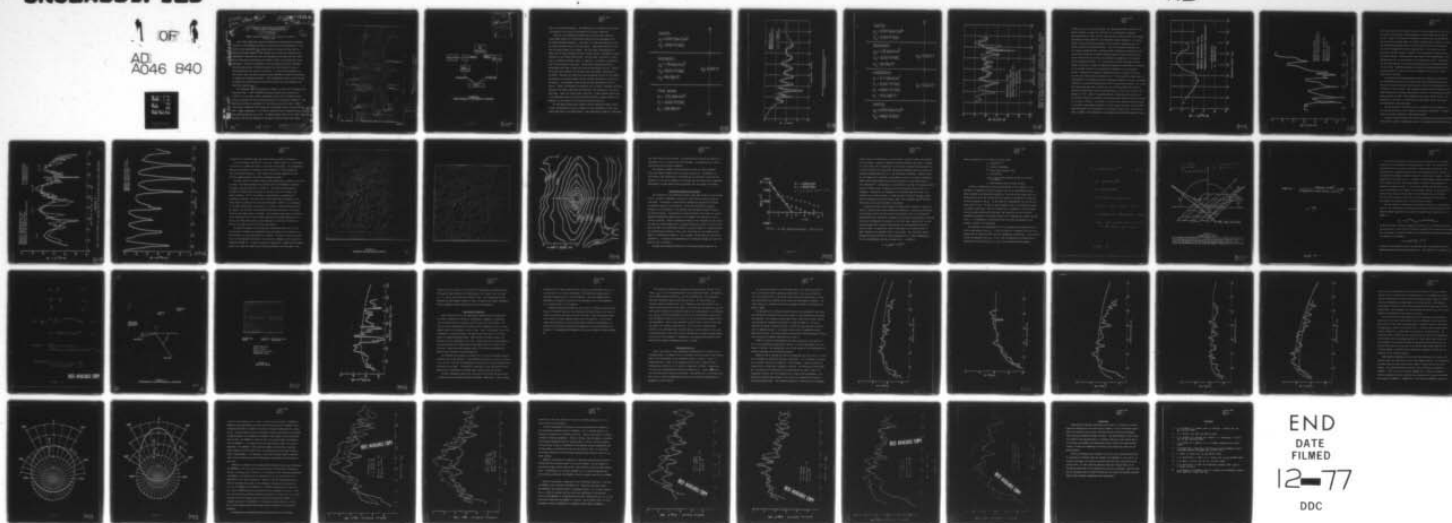
TEXAS UNIV AT AUSTIN DEFENSE RESEARCH LAB
A SUMMARY ON REFLECTION AND SCATTERING OF ACOUSTIC WAVES FROM M--ETC(U)
MAR 67 G R BARNARD

F/G 17/1

UNCLASSIFIED

NL

1 OF 1
AD
A046 840



END
DATE
FILMED
12-77
DDC

1672B1
Please retain

MOST Project - 21622K
7 Mar 1967
GRB:sv

52P/622C, J

(6) A SUMMARY ON REFLECTION AND SCATTERING OF
ACOUSTIC WAVES FROM MODEL SURFACES

(10) G. R./Barnard

Defense Research Laboratory, The University of Texas -
Austin, Texas

(1) NW

Since 1960, the Defense Research Laboratory has been working on problems related to reflection and scattering of sound from the ocean boundaries. This work has been sponsored by the United States Navy Bureau of Ships, now the Naval Ship Systems Command. These studies have included both analytical and experimental investigations, with the experimental work being done in a laboratory tank which has provisions for precise control of the parameters of the experiment. Full-scale experiments at sea are expensive and time consuming, and particular aspects of reflection theory are often obscured by sea or bottom conditions that cannot be controlled. The small-scale experiments in the acoustic tank with model surfaces provide information rapidly and accurately to compare with mathematical models. These mathematical models can then be used to predict the reflection and scattering of sound by the ocean boundaries for full-scale conditions.

The laboratory tank, as illustrated in SLIDE 1 is eight feet in diameter and seven feet deep. A dual transducer positioning system with an accuracy of ± 0.003 in. in the three spatial coordinates, and 0.1 deg in azimuth and tilt allows the geometry of the scattering situation to be accurately controlled. The model being studied is suspended on a tray from the top of the tank. SLIDE 2 illustrates a simplified block diagram of the equipment used in the experimental work. Signal measurements in the tank are made with short sinusoidal pulses so that standing waves are not set up. To ensure several cycles of the signal in the pulse, the carrier frequency of the pulse is usually higher than signals

AD A046840

DDC FILE COPY

NOV 29 1977

DISTRIBUTION STATEMENT A
Approved for public release;
Distribution Unlimited

107 500

48-2

AD 112



LABORATORY TANK AND INSTRUMENTATION FOR
REFLECTION AND SCATTERING STUDIES

DDC
RECEIVED
NOV 29 1977
A

ACCESSION FOR	
NTIC	White Section <input checked="" type="checkbox"/>
DOB	Bull Section <input type="checkbox"/>
UNANNOUNCED	<input type="checkbox"/>
JUSTIFICATION	
<i>Letter on file</i>	
BY	
DISTRIBUTION/AVAILABILITY CODES	
Dist	AVAIL. AND/OR SPECIAL
A	

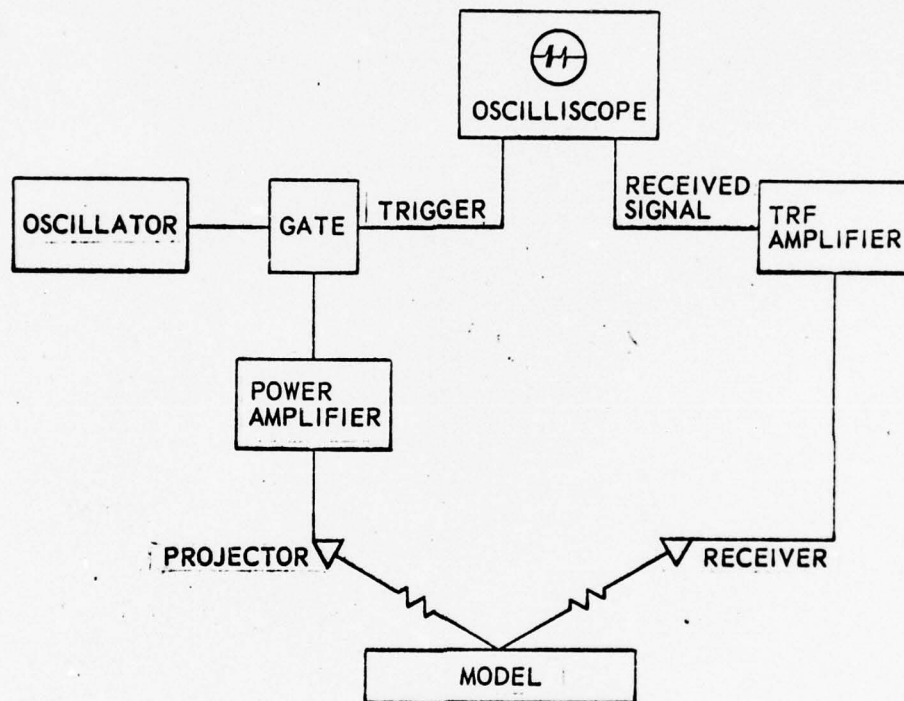


FIGURE 10
BLOCK DIAGRAM OF EXPERIMENTAL EQUIPMENT

SLIDE 2

Date
 DRG. - UT
 DWG AS-66-262-S
 SKM - EJW
 4 - 12 - 66

used in full-scale experiments. The dimensions of the model are scaled with the frequency of the pulse to correspond to full-scale conditions.

Currently, the scattering of plane waves of sound from a family of rough random surfaces is being studied analytically and experimentally at the Defense Research Laboratory. This model is a good representation of the sea surface and many areas of the ocean floor. These model surfaces are the last of several models to be studied. The first model investigated was a plane layer of fluid sediment overlying a layer of sand. This model is representative of some abyssal plain areas. The next model consisted of a plane layer of sediment overlying a layer of limestone. This model is representative of other abyssal plain areas. The analytical methods described by Brekhovskikh were found to agree well with the experimental results. SLIDE 3 illustrates the parameters for the model with the sediment overlying sand, and SLIDE 4 indicates the theoretical and experimental results for this model. The abscissa is the grazing angle and the ordinate represents the reflection coefficient. The agreement of the theoretical and experimental results is obvious. SLIDE 5 illustrates the parameters for the model of sediment overlying limestone, and SLIDE 6 indicates the theoretical and experimental results for this model. Again, the results agree quite well. A more complete description of the experiments and the results have been reported by Barnard, Bardin, and Hemphins¹ in the Journal of the Acoustical Society of America.

The next model studied was a pressure release sinusoidal surface, which is most representative of the sea surface but also corresponds to some ocean bottom areas such as the Blake Plateau. The scattering of sound by a sinusoidal

WATER:

$$\rho_3 = 0.997 \text{ GM/CM}^3$$

$$C_3 = 4925 \text{ FT/SEC}$$

SEDIMENT:

$$\rho_2 = 1.78 \text{ GM/CM}^3$$

$$C_2 = 5023 \text{ FT/SEC}$$

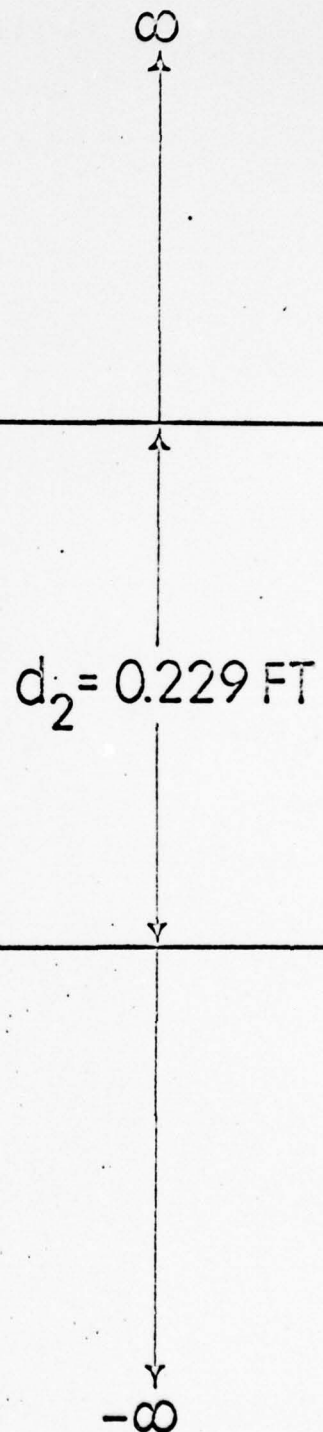
$$\alpha_2 = 8.0 \text{ DB/FT}$$

FINE SAND:

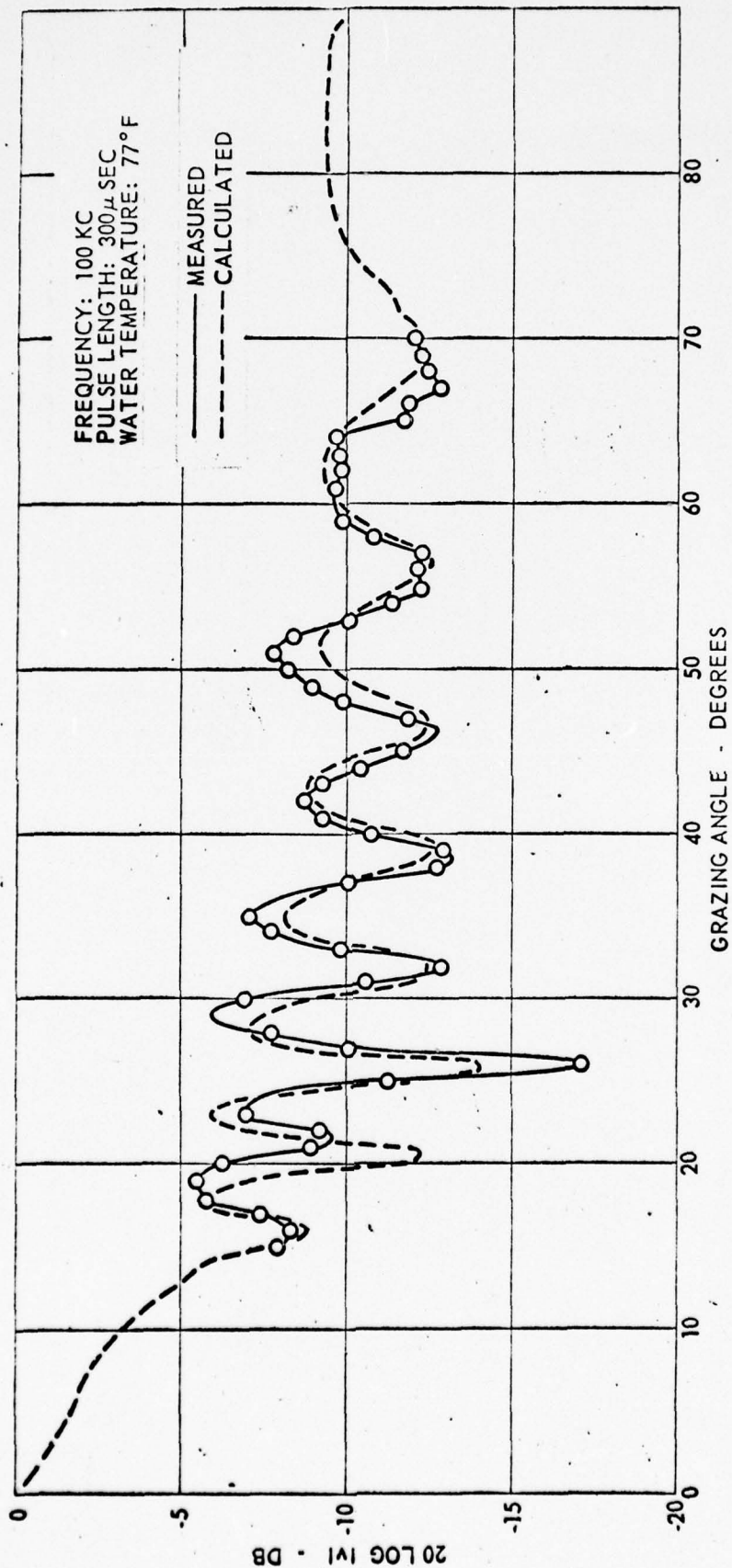
$$\rho_1 = 1.92 \text{ GM/CM}^3$$

$$C_1 = 5435 \text{ FT/SEC}$$

$$\alpha_1 = 18.8 \text{ DB/FT}$$



SLIDE 3



REFLECTION COEFFICIENT VERSUS GRAZING ANGLE FOR
 A FLUID SEDIMENT OVERLYING SAND

SLIDE 4

WATER:

$$\rho_3 = 0.997 \text{ GM/CM}^3$$

$$C_3 = 4925 \text{ FT/SEC}$$

SEDIMENT:

$$\rho_2 = 1.78 \text{ GM/CM}^3$$

$$C_2 = 5023 \text{ FT/SEC}$$

$$\alpha_2 = 8.0 \text{ DB/FT}$$

$$d_2 = 0.208 \text{ FT}$$

LIMESTONE:

$$\rho_1 = 2.11 \text{ GM/CM}^3$$

$$C_1 = 8156 \text{ FT/SEC}$$

$$b_1 = 4980 \text{ FT/SEC}$$

$$\alpha_1 = 15.0 \text{ DB/FT}$$

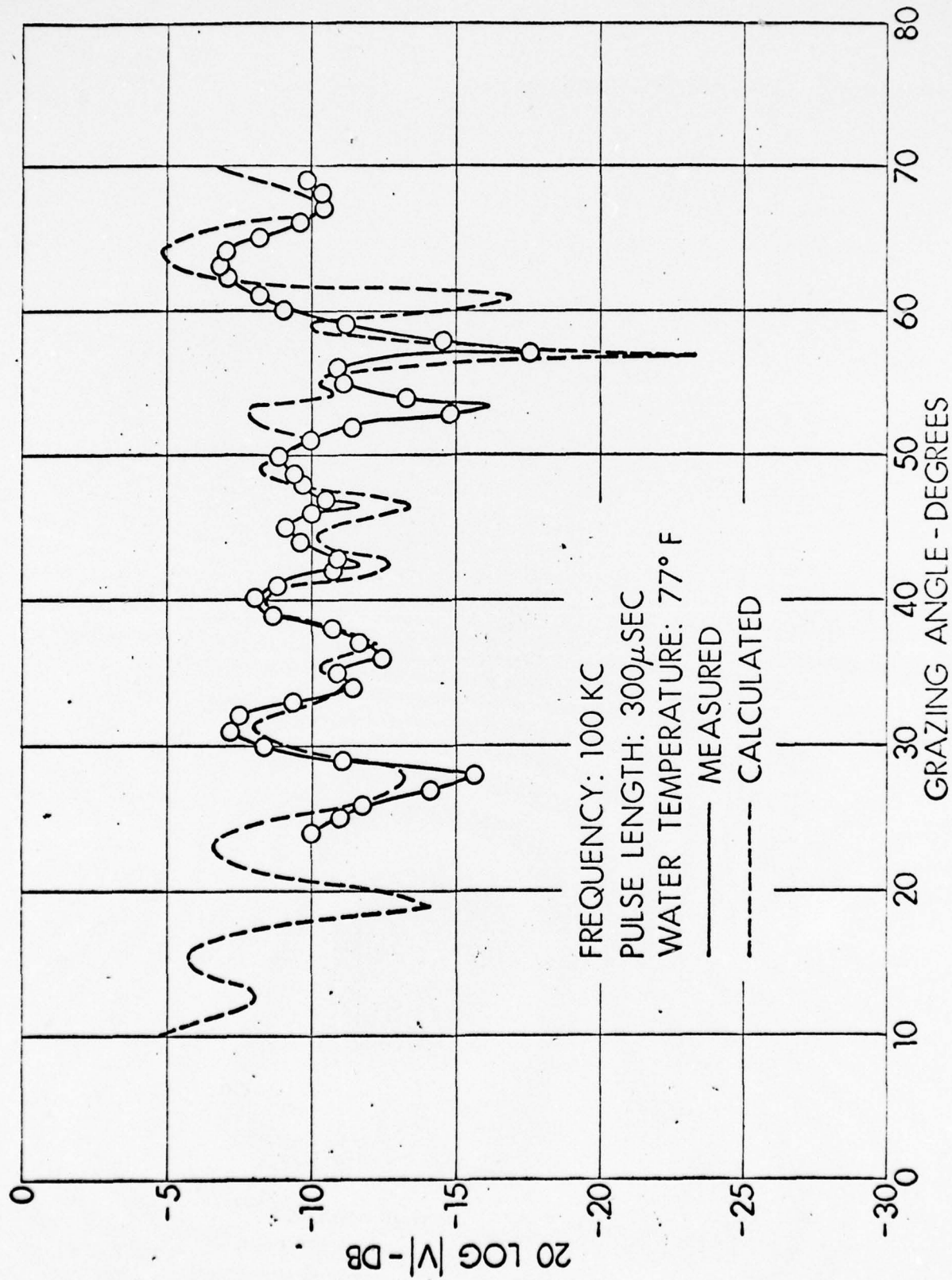
$$d_1 = 0.250 \text{ FT}$$

WATER:

$$\rho_3 = 0.997 \text{ GM/CM}^3$$

$$C_3 = 4925 \text{ FT/SEC}$$

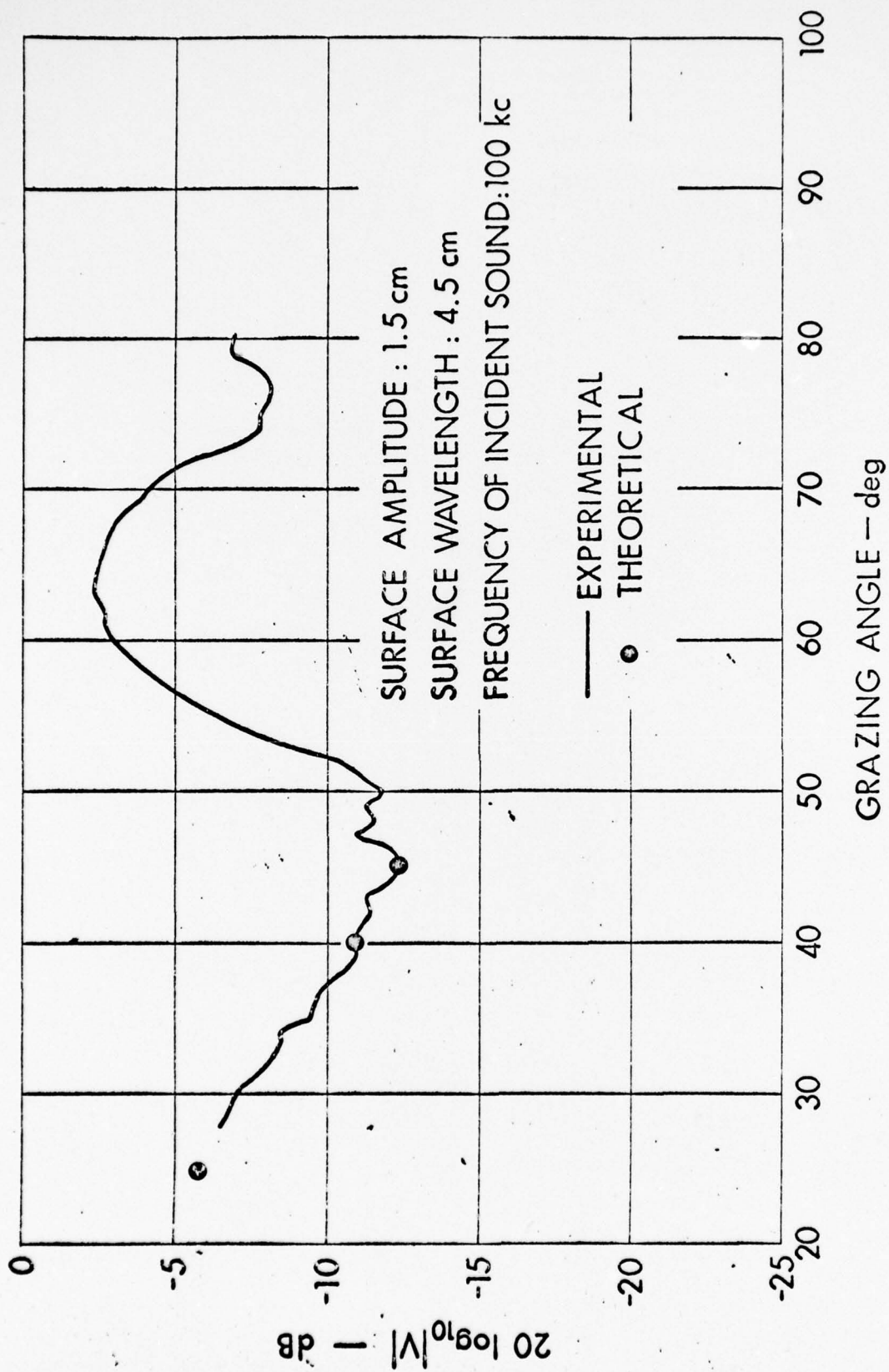
SLIDE 5

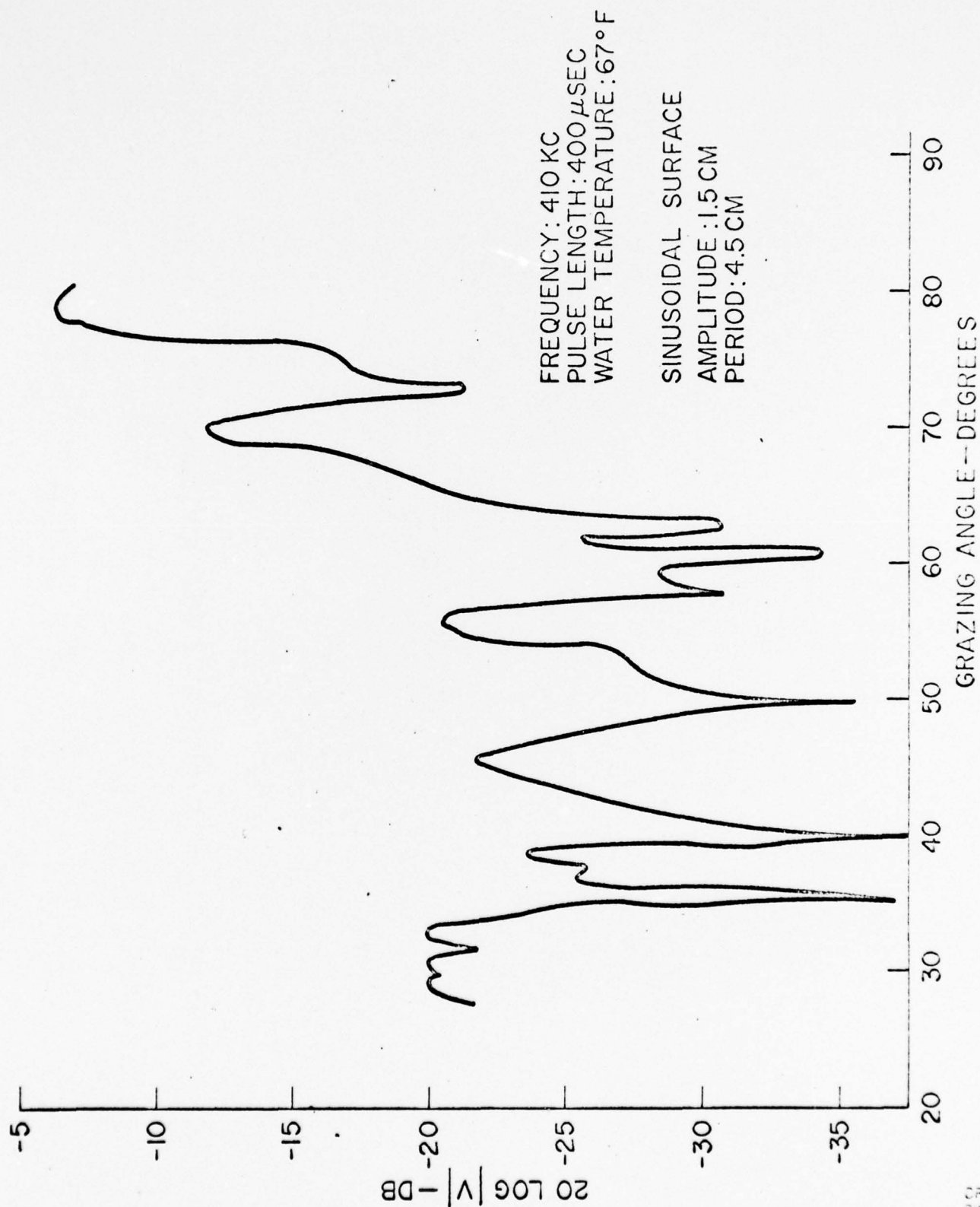


REFLECTION COEFFICIENT VERSUS GRAZING ANGLE
FOR A FLUID SEDIMENT OVERLYING LIMESTONE

SLJ DE 6

surface was first studied by Rayleigh. He obtained amplitude coefficients for normal incidence in terms of an infinite set of simultaneous equations. Rayleigh was able to solve this set only with the restriction that the incident wavelength be large compared to the sinusoidal surface amplitude. In the past decade, several papers have appeared in the literature concerning the scattering of sound by sinusoidal surfaces. Most of the theories advanced thus far contain assumptions that in general provide inadequate descriptions of the reflection of sound from a simple sinusoidal pressure release surface unless severe restrictions are placed on the geometrical parameters of the sinusoid and the frequency involved. In a recent paper, Uretsky² described an exact method of solution. He made no simplifying assumptions concerning the frequency of the incident radiation or the geometrical parameters of the sinusoidal surface. Techniques for numerical computation were not stressed by Uretsky but have since been reported by Barnard et al.³ The sinusoidal surface studied experimentally at the Defense Research Laboratory was made by cutting a sinusoidal variation in a piece of styrofoam about 120 cm. on each side and about 7 cm. thick. This cutting was done with a special tool on a milling machine and produced a sinusoidal surface with a peak to peak amplitude of 3.0 cm. and a surface wavelength of 4.5 cm. SLIDE 7 is experimental data illustrating the variation of the specular reflection coefficient with grazing angle when the carrier frequency of the pulse is 100 kHz. At 100 kHz, the ratio of the incident sound wavelength to the peak to peak surface amplitude is about 0.5, and the ratio of the incident sound wavelength to the wavelength of the surface is about 0.34. For the data shown in SLIDE 8, the frequency of the incident pulse was 400 kHz where the ratio





SPECULAR REFLECTION FROM A SINUSOIDAL SURFACE

SLIDE 8

DRP - 1 CT
 ENG AS9820
 GRB-1 KKK
 9-22-64

of the wavelength of the incident sound to the surface amplitude is 0.12, and the ratio of the incident sound wavelength to the wavelength of the surface is 0.09. SLIDE 9 illustrates the comparison of theoretical and experimental results for the situation where the incident grazing angle is fixed at 45 deg and the reflected grazing angle is varied from about 30 deg to 120 deg with the carrier frequency of the pulse being 100 kHz. It is evident that the scattering from this surface is similar to the scattering one observes from an optical grating. Corrections have been made for the directionality of the hydrophone but not for the projector in the theoretical curves. Corrections for the directionality of the projector should improve the agreement between the two curves. SLIDE 10 illustrates the specular reflection coefficient for a grazing angle of 45 deg as the carrier frequency of the pulse is varied from 70 kHz to 260 kHz.

The generally satisfying agreement between the theoretical predictions and experimental results in the tank work and other comparisons between the results of the model tank work and full-scale results at sea demonstrate the usefulness of the tank work. This agreement between theory and experiment for models having easily defined parameters was the basis for continuing the model scattering work for models whose parameters were not so easily defined. The remainder of this paper is a description of such models and the theoretical and experimental results obtained.

The sea bottom and the surface do not in general have the regularity of the sinusoidal surface so more irregular surfaces were considered. The model chosen for further study was a rough random surface.

A survey of contour maps of the ocean bottom indicated none were sufficiently detailed for a model so aeromagnetic maps of the Northwest Canadian Shield were

INCIDENT GRAZING ANGLE: 45°
 SURFACE AMPLITUDE: 1.5 cm
 SURFACE WAVELENGTH: 4.5 cm
 FREQUENCY OF INCIDENT SOUND: 100 kc

L = SCATTER ORDER
 --- EXPERIMENTAL
 — THEORETICAL

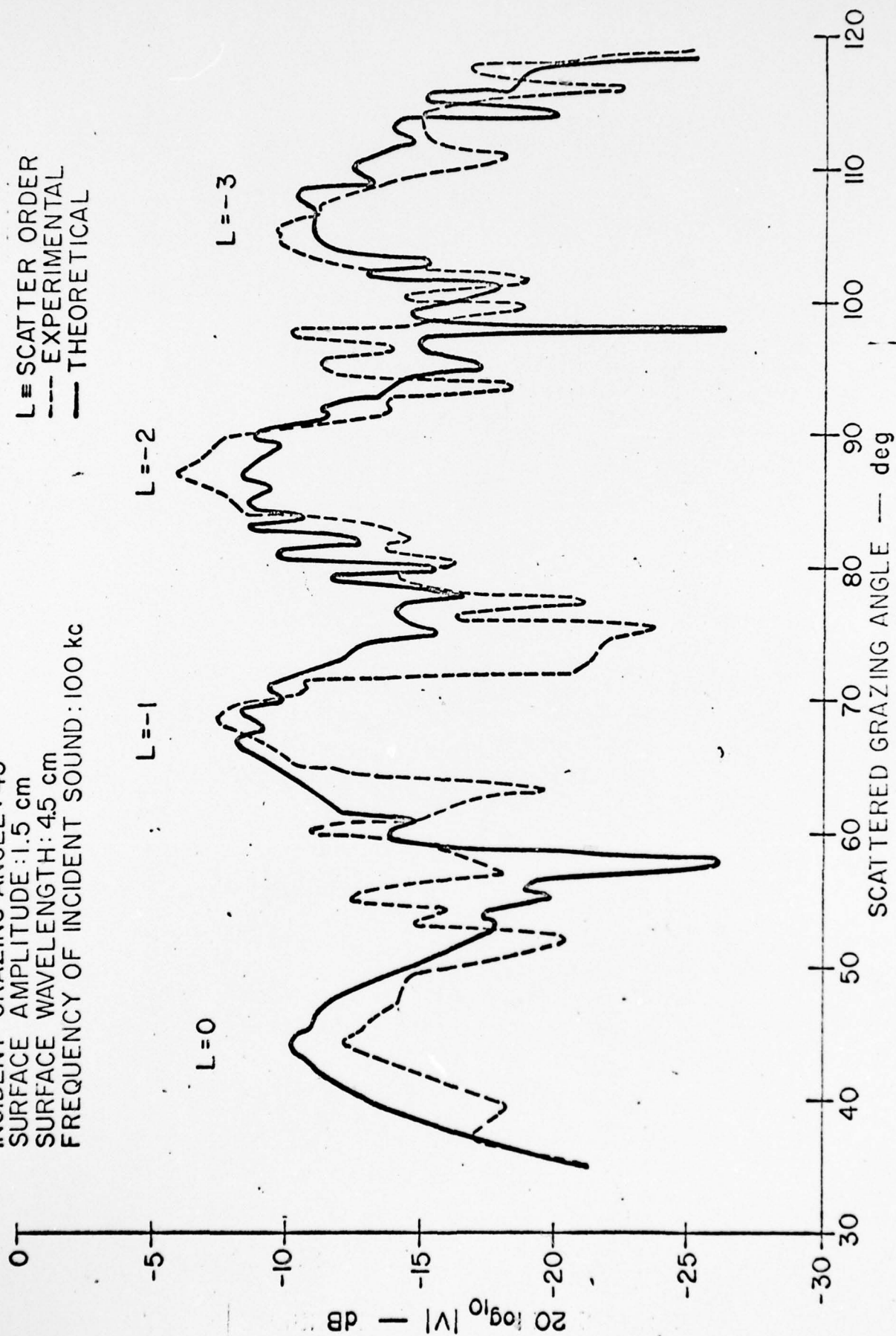


FIGURE 7
 THE SCATTERING OF SOUND BY A PRESSURE-RELEASE SINUSOID

SURFACE AMPLITUDE : 1.5 cm
 SURFACE WAVELENGTH : 4.5 cm
 GRAZING ANGLE : 45°

The graph shows the magnitude of the surface wave reflection coefficient, $20 \log_{10} |V|$ in dB, as a function of frequency in kc. The curve exhibits a series of peaks and nulls, characteristic of a resonant system. The peaks occur at approximately 80, 105, 125, 145, 180, 200, 220, and 250 kc. The nulls occur at approximately 95, 115, 135, 155, 175, 195, 215, and 235 kc. The magnitude generally increases with frequency, starting around -5 dB at 80 kc and reaching approximately -25 dB at 250 kc.

SLIDE 10

interpreted as topological maps and yielded surfaces suitable for modeling.

Four of the maps, each 40.6 cm x 40.6 cm, scaled 1.58 cm to the kilometer, in the form of a square were used as the pattern for the model. The aeromagnetic maps were the subject of a previous study by Horton et al⁴ which determined their statistical properties. This earlier work concerned applying the statistical considerations to the study of geological studies.

The model is 85 cm in length along an edge representing a distance of 51.5 km on a map. The height dimension was converted from the aeromagnetic dimension, the gamma, using the scale $10 \gamma = 0.0795$ cm. The contours on the map were located on the model with an accuracy of 0.19 mm in each of the three coordinate variables. This is an accuracy of approximately one hundredth of a wavelength at 100 kHz. The total relief of the model from the highest to the lowest points is slightly less than four wavelengths. SLIDE 11 is a photograph of the model surface used in the studies. In order to avoid difficulties from the edges of the surfaces, the insonified region was restricted to the central fourth of the surface which is outlined. The elliptical curve shows the location of the half-power level of the incident beam when the incident grazing angle is 45 deg. The small black square is one wavelength on each side at 100 kHz so that one can judge the size of the hills and valleys.

The specific formulas for the scattering coefficients which will be used in this paper to compare with experimental data are based on the assumption that the statistics of the rough surface are isotropic. In order to test this assumption, the autocovariance function of the surface was computed and the values are contoured on SLIDE 12. In order to make this computation, a square grid of sample points $\frac{1}{2}$ in. apart was drawn on the central one-fourth of the four maps. This

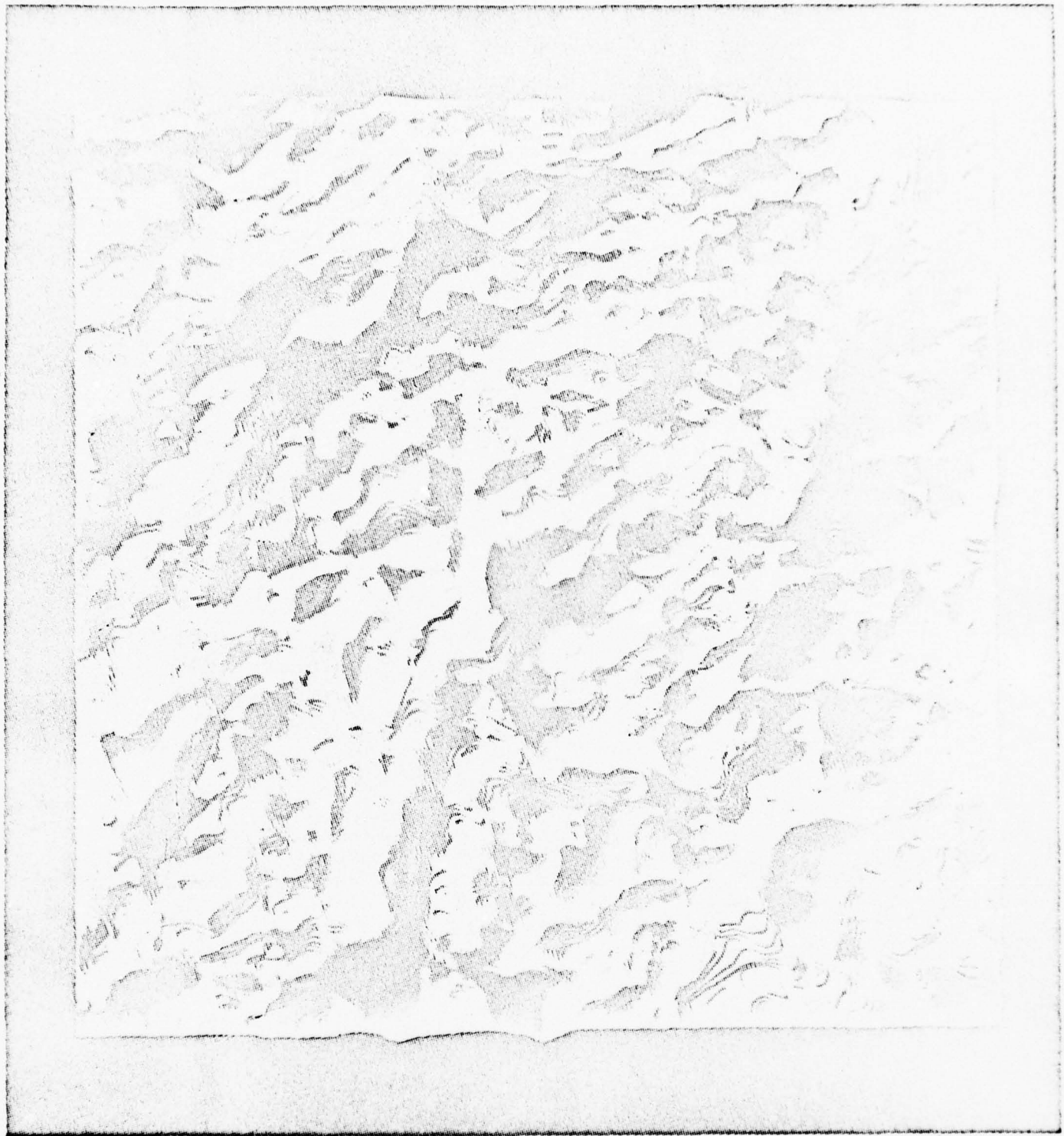
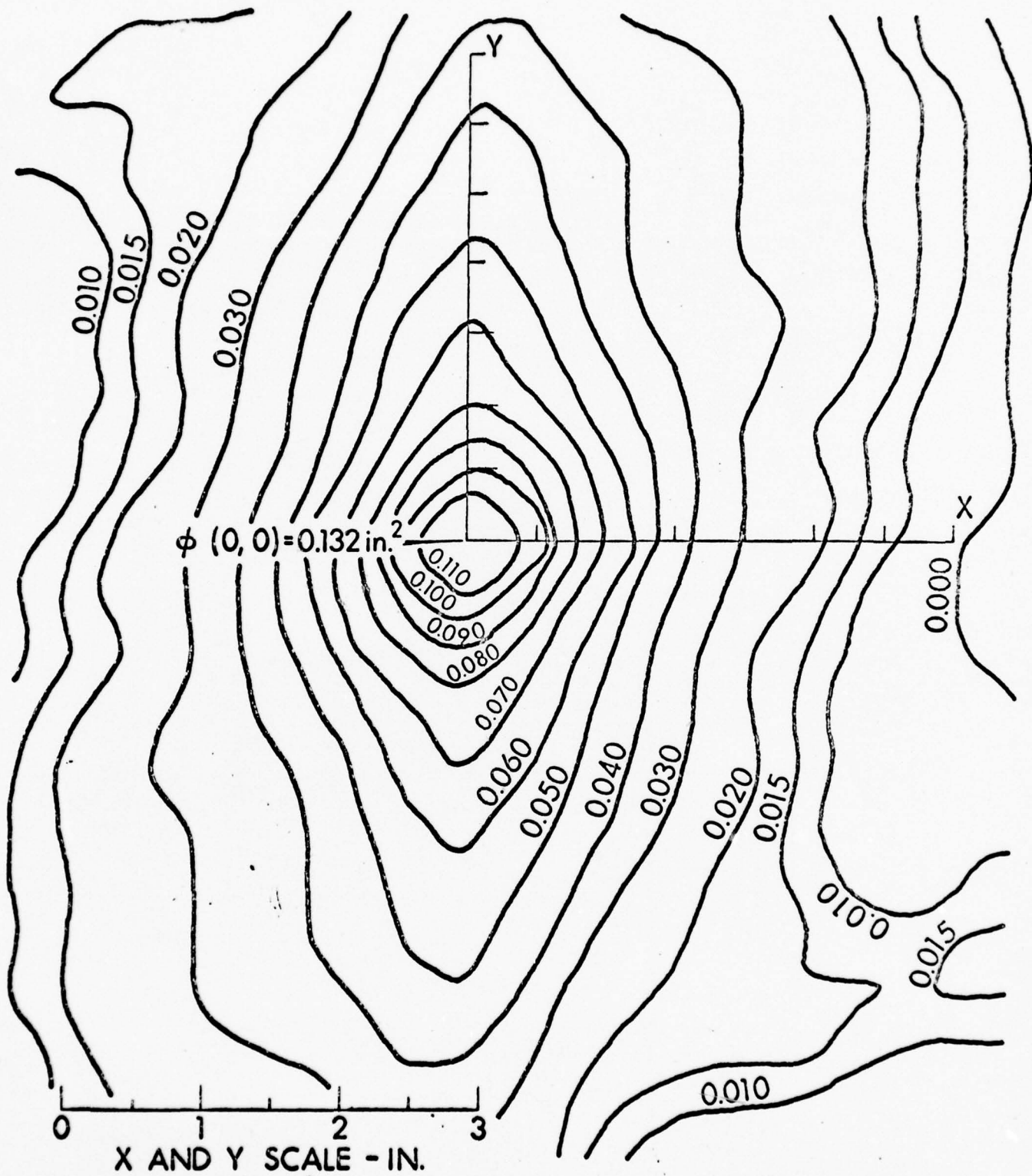


FIGURE 9 //

PRESSURE-RELEASE RANDOM SURFACE





SLIDE 12

DRL - UT
DWGAS-66-946
SKM - RFO
9 - 16 - 66

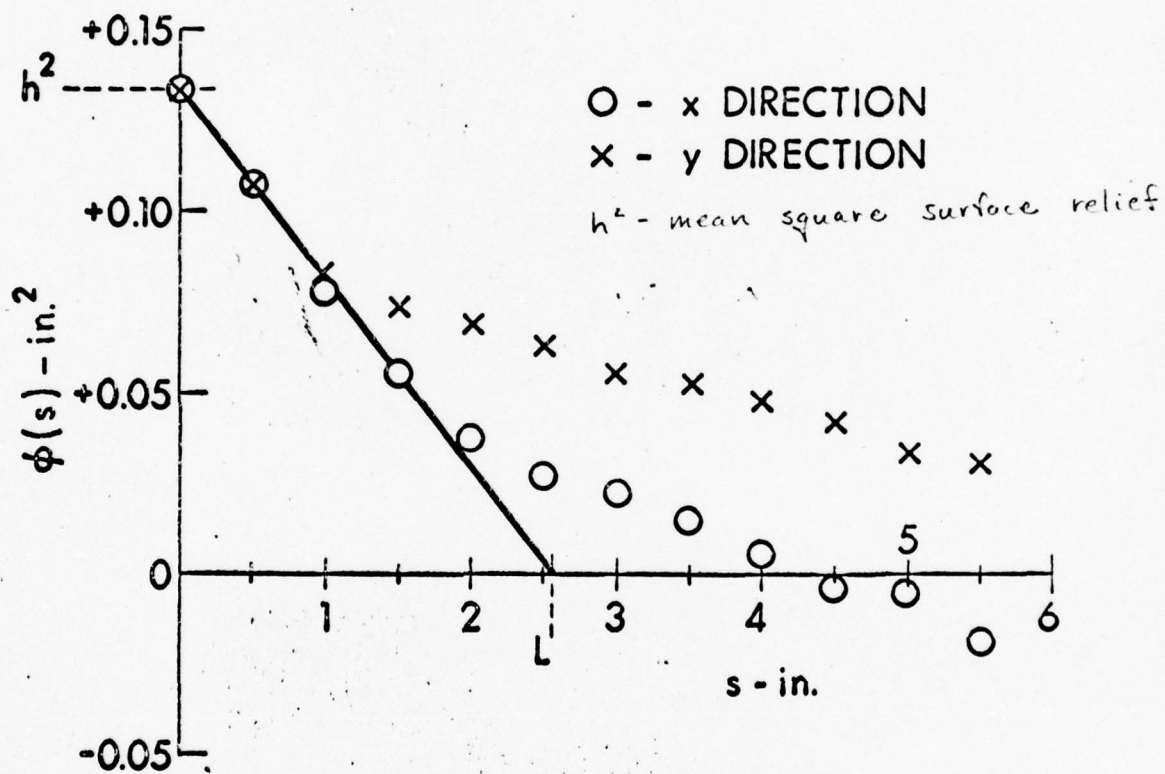
gave 1089 values of the elevation. The autocovariance function was computed at intervals of $\frac{1}{2}$ in. in each of the two coordinates. The formulas used in this calculation have been given elsewhere.

The contours in SLIDE 12 are essentially circular for small distances while they become elongated ovals for larger separations. Fortunately, the scattering at high frequencies is determined by the curvature of the hills and valleys so it is only the shape of the contours near the origin that is important. Consequently, one may assume without hesitation that the surface is isotropic.

Theoretical Formulas for the Model

The literature on the reflection of waves from rough surfaces is quite extensive so it would be impossible to provide a useful guide within the limits of this paper. Fortunately, a recent book by Beckmann and Spizzichino⁵ provides an excellent survey of the literature. Of the many theoretical solutions available in the literature, it was decided that the paper by Eckart⁶ offered the greatest promise. His solution is easily evaluated, and it does not require elaborate mathematical analysis such as, for example, the solution of a set of infinite equations. Eckart's assumptions related to the statistics of the surface are that the surface heights have a gaussian distribution, which is valid for this model and that the autocovariance function of surface heights is of gaussian form. The autocovariance functions in the x and y directions for this random surface model are illustrated in SLIDE 13. As is evident, the functions are more nearly exponential. A straight line approximation is illustrated through the first four points in the x direction.

Although the statistical properties of the present model surface do not



PROFILE OF THE AUTOCORRELATION FUNCTION

SLIDE 13

satisfy exactly the assumptions on which Eckart's theory is based, the agreement is close enough to justify a comparison between experiment and theory. Actually it is not likely that the departure of the surface statistics from gaussian statistics will affect the theoretical calculations seriously until one attempts to calculate standard deviation for σ , the scattering coefficient. Another reason for the appeal of his solution to the authors is that it is based on Helmholtz's formula which has provided very practical formulas for other applications at this laboratory^{7,8}. Consequently, it was decided to use and, if necessary, modify Eckart's solution unless disagreement with the experiment required that it be abandoned. Fortunately, the agreement is sufficiently good that there is no incentive to try other theories. A paper by Horton and Muir⁹ contains several explicit formulas derived from Eckart's work, and a companion paper¹⁰ provides more detail of the work described in this paper.

The Horton and Muir paper concerns the application of Eckart's scattering theory to surfaces with various statistical properties. Scattering coefficients are developed for both the low and the high frequency cases for isotropically rough surfaces with exponential, gaussian, and sinusoidal autocovariance functions. The specific assumptions of interest for the model under consideration are that surface heights have a gaussian distribution, the autocovariance function of surface heights is exponential, and the wavelength of the incident sound is small compared to the maximum relief of the surface. The scattering formula obtained by Horton and Muir for these assumptions with a linear approximation for the autocovariance function is shown as Eq. 1 in SLIDE 14,

$$\sigma = \sigma_0 \left[(k h c)^4 + w^2 \right]^{-3/2},$$

where the parameters of the equation are also shown.

$$\sigma_0 = 1/8\pi(k^2 h L c^2)^2$$

k = radiation wavenumber

h^2 = mean square surface relief

$$w = (kL)^2(a^2 + b^2)$$

a, b, c = sums of the direction cosines of the source and receiver

L = autocovariance decay function distance

In order to examine more easily the predictions of this solution, it is desirable to introduce the actual variables used in the experimental studies. These variables are illustrated in SLIDE 15. The source P was always held at a fixed position in the $(x,)$ plane while the receiver R was moved by varying one of the two angles, θ_r and ϕ_r . In the majority of measurements, θ_r was held constant equal to zero. In terms of these variables, some of the direction cosines are shown on this slide. When the formula for σ is expanded in these variables with the further specification that $\theta_r = 0$, the expression for the scattering coefficient becomes Eq. 2 on SLIDE 16 where G is a dimensionless constant defined by Eq. 3. The parameter G characterizes the relief and the coherence of the surface in terms of the wavelength.

The subscript T has been applied to σ to distinguish this theoretical value from the experimental value σ_E . It will be shown on a subsequent slide that this formula does not agree very well with the experimental observations. In particular, σ_T does not approach zero as $\phi_r \rightarrow 0$ or π , and the maximum in σ_T considered as a function of θ does not occur at $\phi_i = \phi_r$ as the experimental data suggests.

$$\sigma = \sigma_0 \left[(k h c)^4 + w^2 \right]^{-3/2}$$

Egn 1.

$$\sigma_0 = \frac{1}{8\pi} (k^2 h L c^2)^2$$

$$w = (kL)^2 (a^2 + b^2)$$

k = radiation wavenumber

h^2 = mean square surface relief

L = autocovariance decay function distance

a, b, c - sums of the direction cosines
of the source and receiver

SLIDE 14

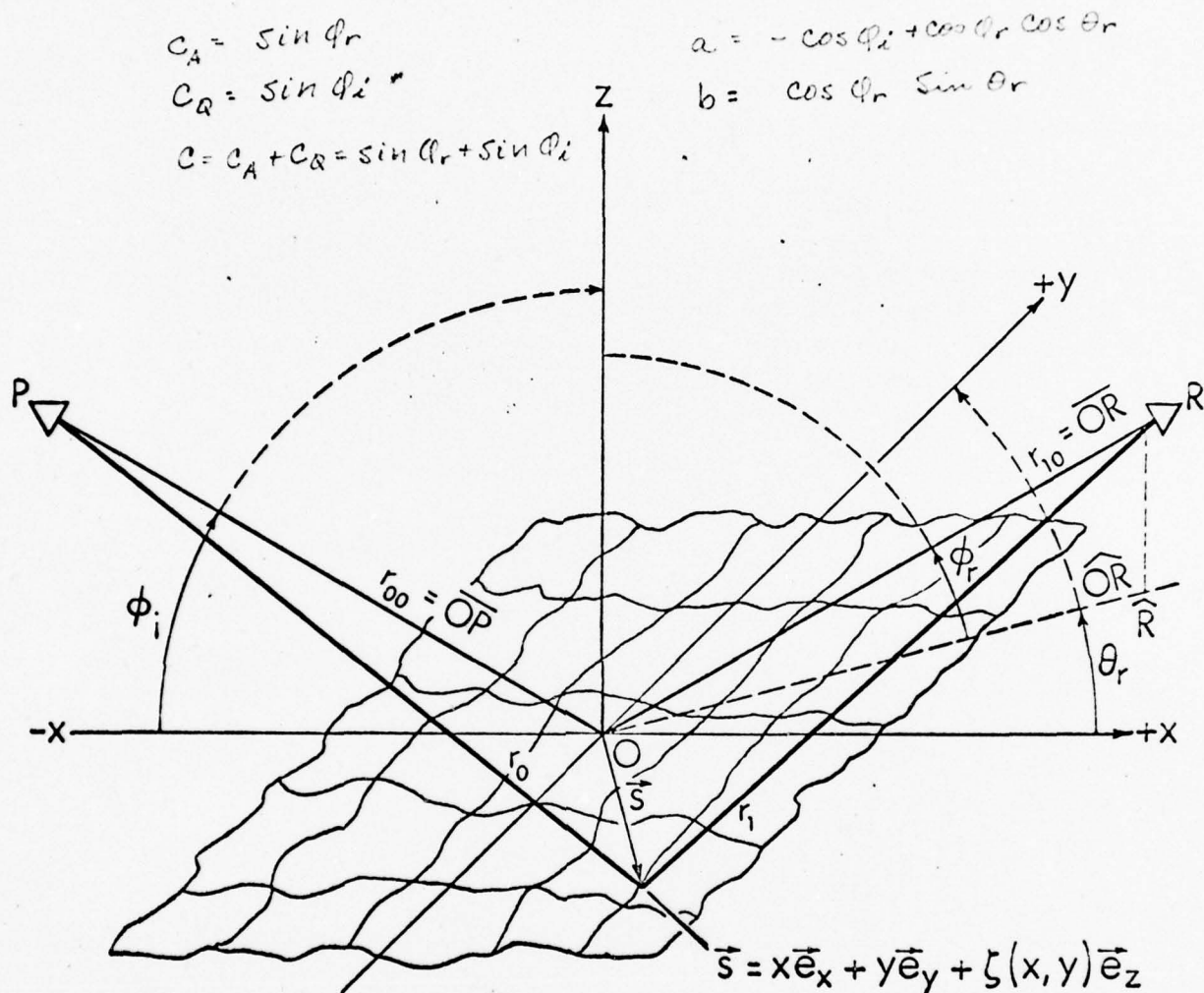


FIGURE 2 15
CO-ORDINATE SYSTEM

THE INTERFACE IS POSITIONED WITH ITS AVERAGE ON THE x - y PLANE. THE AXIS OF THE INCIDENT BEAM, \overline{OP} , LIES IN THE x - z PLANE AT AN ANGLE ϕ_i UP FROM THE $-x$ AXIS. THE LINE FROM THE ORIGIN TO THE RECEIVER, \overline{OR} , MAKES AN ANGLE OF ϕ_r WITH THE x - y PLANE; ITS PROJECTION ON THE x - y PLANE, \widehat{OR} , MAKES AN ANGLE OF θ_r WITH THE x AXIS.

$$\sigma_T(\varphi_i, \varphi_r) = \frac{G(\sin \varphi_r + \sin \varphi_i)^4}{8\pi \left\{ G^2(\sin \varphi_r + \sin \varphi_i)^4 + (\cos \varphi_r - \cos \varphi_i)^2 \right\}^{3/2}} \quad \text{Egn. 2}$$

$$G = \frac{kh^2}{L} \quad \text{Egn. 23}$$

This serious disagreement between theory and experiment led to a renewed examination of the assumptions underlying Eckart's theory. Mr. Mitchell, who performed much of this work for his Master's degree thesis noticed that significantly better agreement between theory and experiment would be obtained if one changed the boundary condition on $\partial p_1 / \partial n$ in the Helmholtz integral. Eckart suggested that one could use Eq. 4 on SLIDE 17 on the pressure release surface, but he pointed out that "in the deep shadows it would be more reasonable to suppose" the condition of Eq. 5. This latter condition implies that the pressure field vanishes at the surface in the shadowed regions. On the surface of strong relief, like the present model, both conditions exist on different portions of the surface so that one is in closer agreement with the facts if one assumes the condition of Eq. 6 over the entire surface.

When the analysis is modified by this boundary condition on the scattered wave, P_1 , the only change in the expression obtained by Horton and Muir for the general integral equation for the scattered pressure field, shown as Eq. 7 in SLIDE 17,

$$4\pi p_1 = ikc(e^{ikr_{10}}/r_{10}) \iint P e^{-ik(ax+by+Cz)} dx dy$$

is that the factor C should be changed to C_A where C_A is the direction cosine of the source and C is the sum of the direction cosines of the source and the receiver. When this change is followed through to the equation for the scattering coefficient, it becomes Eq. 8 in SLIDE 17,

$$\sigma_M = \sigma_0 [(kh)^4 C^2 C_A^2 + w^2]^{-3/2}.$$

In terms of the variables shown in the previous slide, the expression for the modified scattering coefficient becomes Eq. 9. The subscript M is added to σ to

$$\frac{\partial P_i}{\partial n} = \frac{\partial P_o}{\partial n}$$

Egn. 4

$$\frac{\partial P_i}{\partial n} = - \frac{\partial P_o}{\partial n}$$

Egn. 5.

$$\frac{\partial P_i}{\partial n} = 0$$

Egn. 6

$$\Delta \pi p_i = \frac{ike}{r_{io}} e^{ikr_{io}} \iint P e^{-ik(ax+by+cz)} dx dy$$

Egn 7

$$\sigma_m = \sigma_o [(kh)^4 c^2 c_A^2 + w^2]^{-3/2}$$

Egn. 8

$$\sigma_m(\phi_i, \phi_r) = \frac{G(\sin \phi_r + \sin \phi_i)^2 \sin^2 \phi_r}{8\pi \{G^2(\sin \phi_r + \sin \phi_i)^2 + (\cos \phi_r - \cos \phi_i)^2\}^{3/2}}$$

Egn. 9

$$\sigma_m(\phi_i, \phi_r, \theta_r) = \frac{G}{[G^2 + \{(a^2 + b^2)/c^4\}]^{3/2}} \cdot \frac{c_A^2}{8\pi c^4}$$

Egn. 10

BEST AVAILABLE COPY

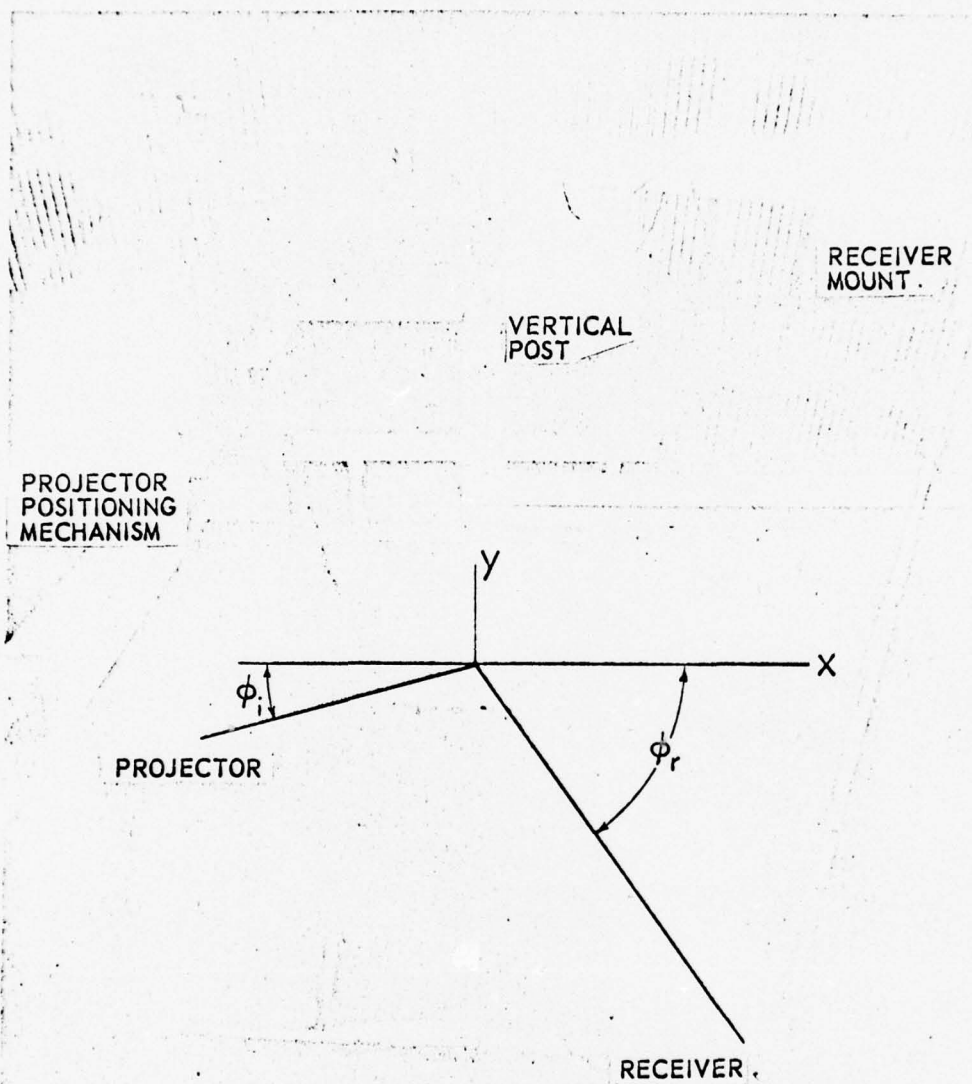
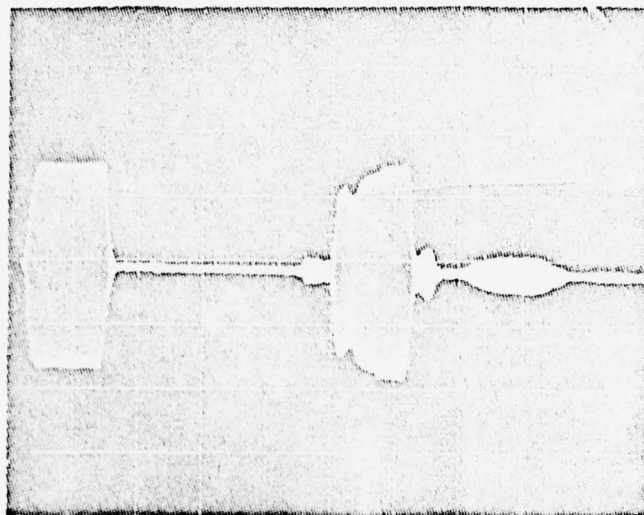


FIGURE 18
PHOTOGRAPH OF THE EXPERIMENTAL APPARATUS



TRANSMITTED
PULSE

MEASURED
PULSE

SCATTERING FROM
TANK WALLS

SPEED: $500 \mu\text{sec}/\text{div}$

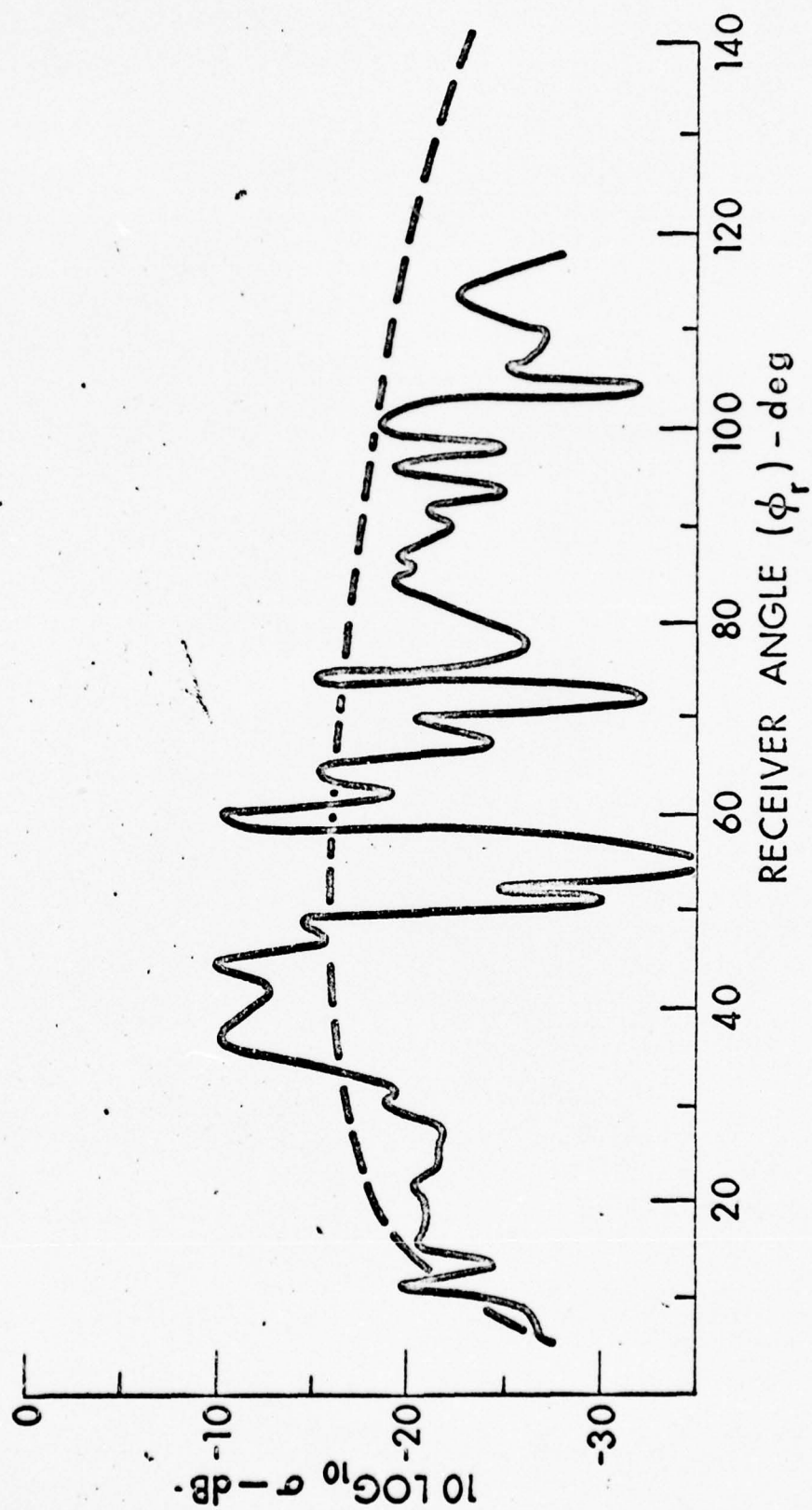
SCALE: $0.2 \text{ V}/\text{div}$

PULSE LENGTH: $700 \mu\text{sec}$

FREQUENCY: 100 kHz

FIGURE 19
RECEIVED PULSE

DRL . . . UT
DWG AS-66-350
SKM . . . EJW
4 - 12 - 66



DRL - UT
DWGAS-66-938
SKM - RFO
9 - 15 - 66

SLIDE 20

indicate that this formula is obtained from a modification of Eckart's theory. The general formula without the restriction $\theta_r = 0$ is given in Eq. 10 where a , b , c , and C_A were defined on a previous slide. The organization of this equation has been changed slightly in order to separate the angular parameters from the parameter G that characterizes the linear dimensions.

Experimental Procedures

Only a brief account of the experimental procedures will be given here. If further information is desired on experimental equipment or procedures, then the authors would be pleased to provide this after this session. The experiments were performed with the model surface submerged in a water filled, redwood tank 24 ft in diameter and 20 ft high. Since it was easier to move the hydrophone in a horizontal plane, the model surface was fixed in a vertical plane on a weighted mounting frame. SLIDE 18 shows the model surface, the projector, and the hydrophone in the tank. During any one set of measurements, the projector was held constant and the hydrophone moved in a circle in two deg steps. Reflection from different areas of the surface were obtained by shifting the reflecting surface horizontally.

The projector was located at a distance of 1.4 m from the surface measured along the axis of the projector. The hydrophone was moved in a circle of radius 2.31 m in such a way that the hydrophone and projector were always pointed toward the center of the model. The mechanical restraints in the tank restricted the position of the hydrophone to grazing angles between 6 deg and 116 deg.

Circular transducers whose active faces were 0.125 m and 0.06 m were used to produce waves of frequency 100 kHz and 200 kHz, respectively. Each of these

7 March 1967

GRB:sv

Page 11

transducers had a conical beam pattern of 8 deg at the half-power points. It was necessary to use a small hydrophone to avoid spatial averaging that is performed automatically by a large hydrophone. The small omnidirectional hydrophone of diameter 5.2 mm used in the experiments had a broad bandwidth so it could be used at each frequency.

Standard laboratory equipment was used to gate a continuous oscillator for signals of 700 μ sec duration. This produced an acoustic pulse in the water of length 1.05 m which contained 70 cycles at 100 kHz. This gated signal served as the input to a power amplifier which drove the projector. The received signal was amplified by a tuned radio-frequency amplifier and displayed on a cathode ray oscilloscope from which the magnitude of the scattered pulse was measured. A representative photograph of the received signal is shown on SLIDE 19.

The system was calibrated by separating the projector and receiver a distance, r_{cal} , of 3.4 m and orienting them on axis toward each other. The peak-to-peak received voltage was then V_{cal} for this configuration. The transducers were then arranged as shown in the previous slide. For travel path, R_{tp} , measured along the acoustic axes of the transducers from the projector to the specular reflection point on the surface to the receiver, one arrives at V_{tp} , the peak-to-peak voltage of the received signal in this configuration. The distances R_{cal} and R_{tp} are large enough that one can use the inverse square law for pressure amplitudes so long as one is careful to use the same source signals for the two measurements. One can then calculate σ_E which yields a value of unity when the surface is a perfect plane reflector. In the case of a perfect plane reflector, it can be shown that one would obtain a value of unity for the scattering coefficient if the value $J(0,0)$ is normalized to a plane at right angles to the axis of the transducer. Consequently, the quantity that should be compared with the present experimental values is $\sigma/\sin\phi_i$.

Experimental Results

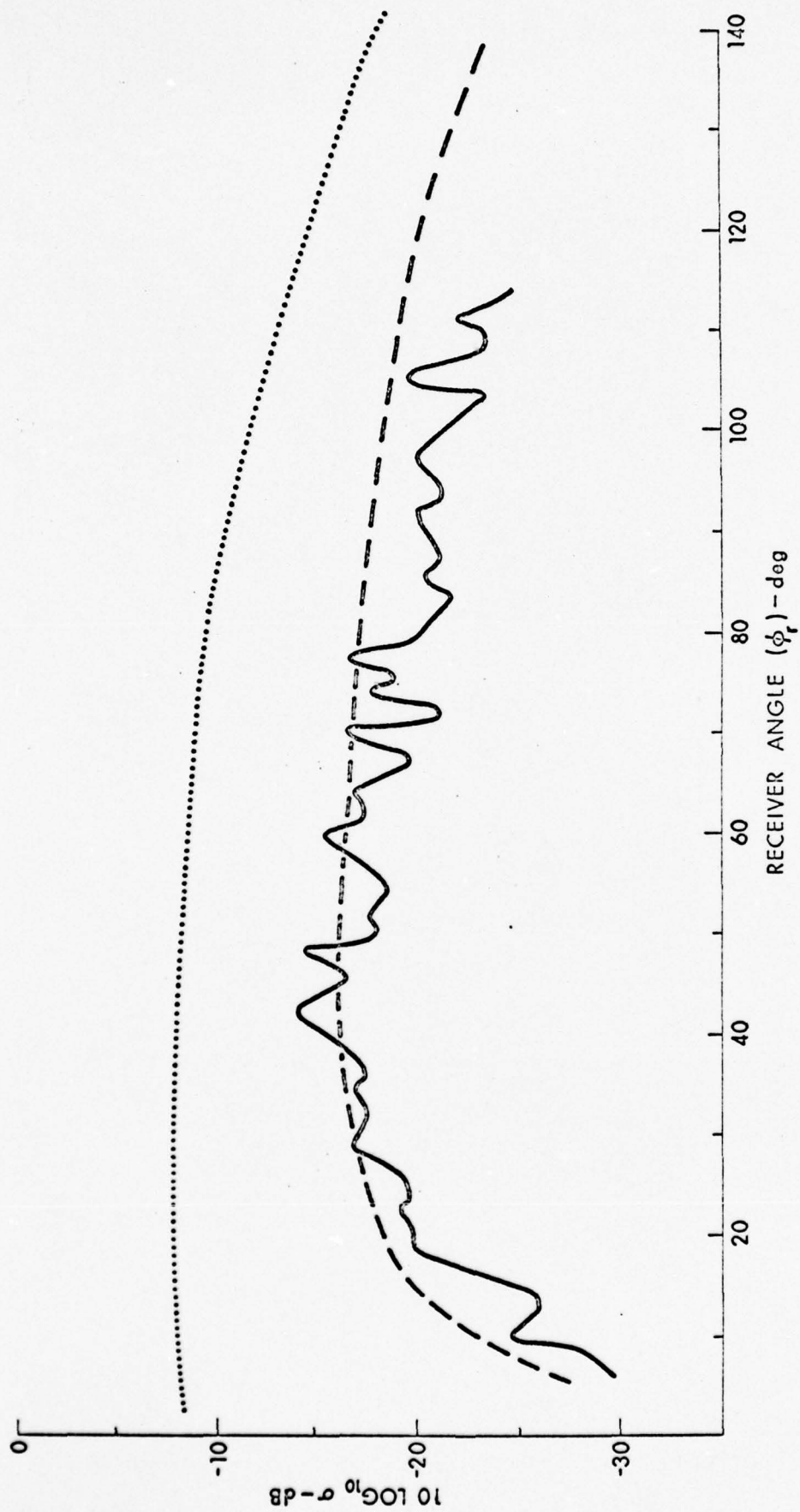
Some of the results of the experimental measurements will be shown on the following slides. On SLIDES 20 to 25, the graphs show the results of the measurements in the plane normal to the scattering surface so that $\theta_r = 0$ and $b = 0$. Consequently Eqs. 1 and 9 can be compared with this data. SLIDE 20 shows a representative curve for $\phi_i = 45$ deg and a frequency of 100 kHz. Measurements were made and σ_E determined for two deg increments of ϕ_i . Large excursions as that occurring near 55 deg were not unusual. The dashed curve is calculated from Eq. 9, and it should be emphasized that there are no arbitrary adjustments of parameters in this equation.

In this slide and each of the following slides, the theoretical quantity that is plotted and labeled scattering coefficient is not the σ_T defined in Eq. 1 nor defined in Eqs. 9 and 10 but these quantities divided by $C_Q (= \sin \phi_i)$. This modification was justified in the section on experimental techniques. The factor $(1/C_Q)$ is a constant for each of the graphs although it may change from graph to graph.

The position of the bottom was moved relative to the position of the source and receiver, and seven more sets of data similar to that presented in this slide were obtained. The average of these eight curves, which gives a better statistical average for comparison with theory, is shown on SLIDE 21. The curve indicated by dashes is computed from Eq. 9, while the curve plotted as circular dots is computed from Eq. 1, the formula derived from the unmodified theory developed by Eckart. This slide contains the empirical evidence mentioned earlier that justifies the boundary condition given in Eq. 6.

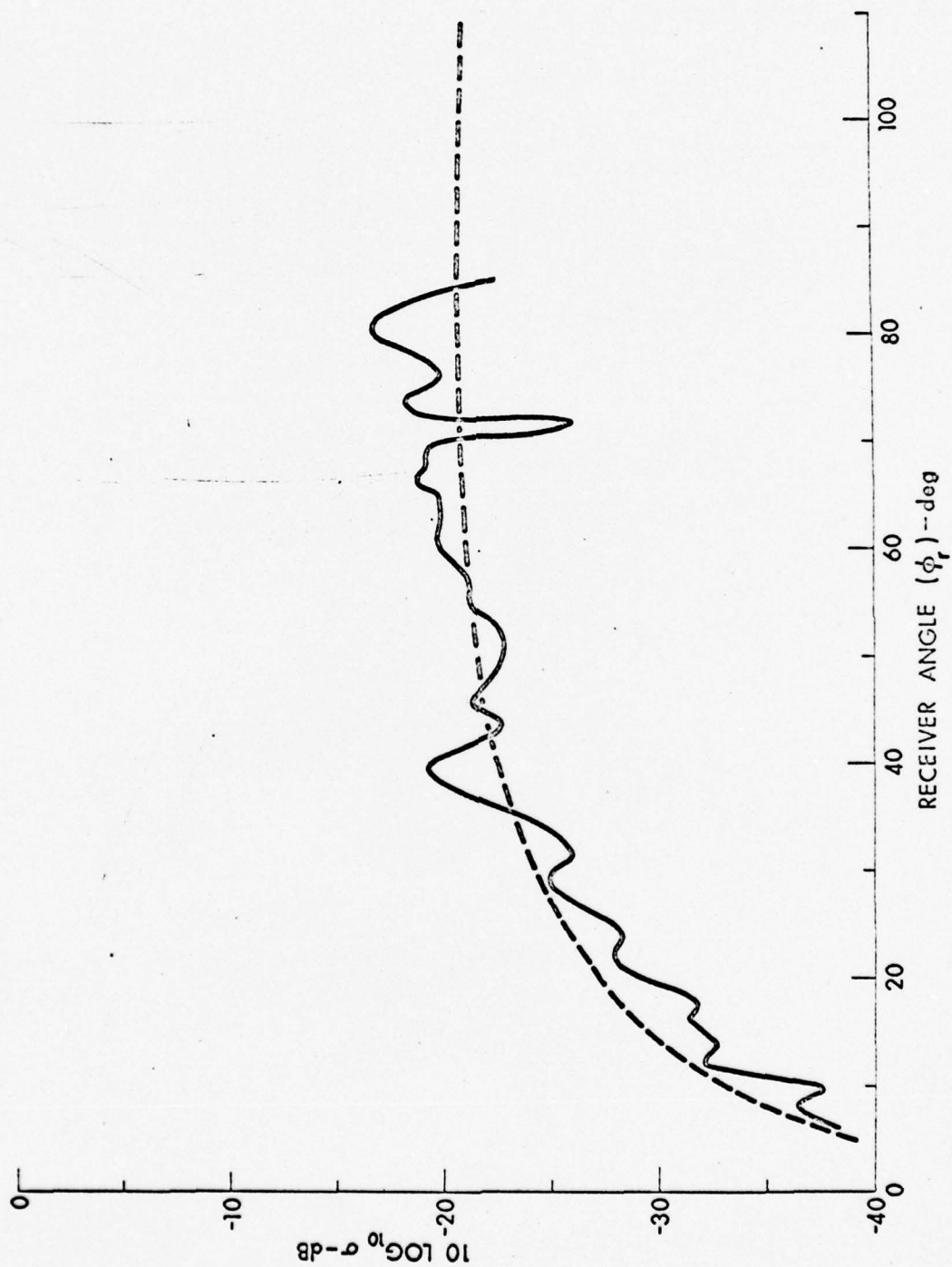
SLIDE 22 contains the experimental data and a theoretical curve based on Eq. 6 for an incident grazing angle of 90 deg, i.e. normal incidence, and a frequency of 100 kHz. The experimental curve is the average of five measurements at different positions on the reflecting surface.

SLIDES 23 and 24 contain the results of experiment and theory for $\phi_i = 40$ deg and a frequency of 100 kHz and 200 kHz, respectively. It is pleasing to see that Eq. 9 predicts correctly the change of σ with frequency. SLIDE 25 contains the results for $\phi = 30$ deg and a frequency of 100 kHz. The theoretical values based Eq. 9 and plotted as a dashed curve are significantly too small. When it is remembered, however, that the surface relief is nearly four wavelengths, it is obvious that significant portions of the valleys are shadowed by the hills at this small grazing angle. This shadowing produces a reduction of the topographic



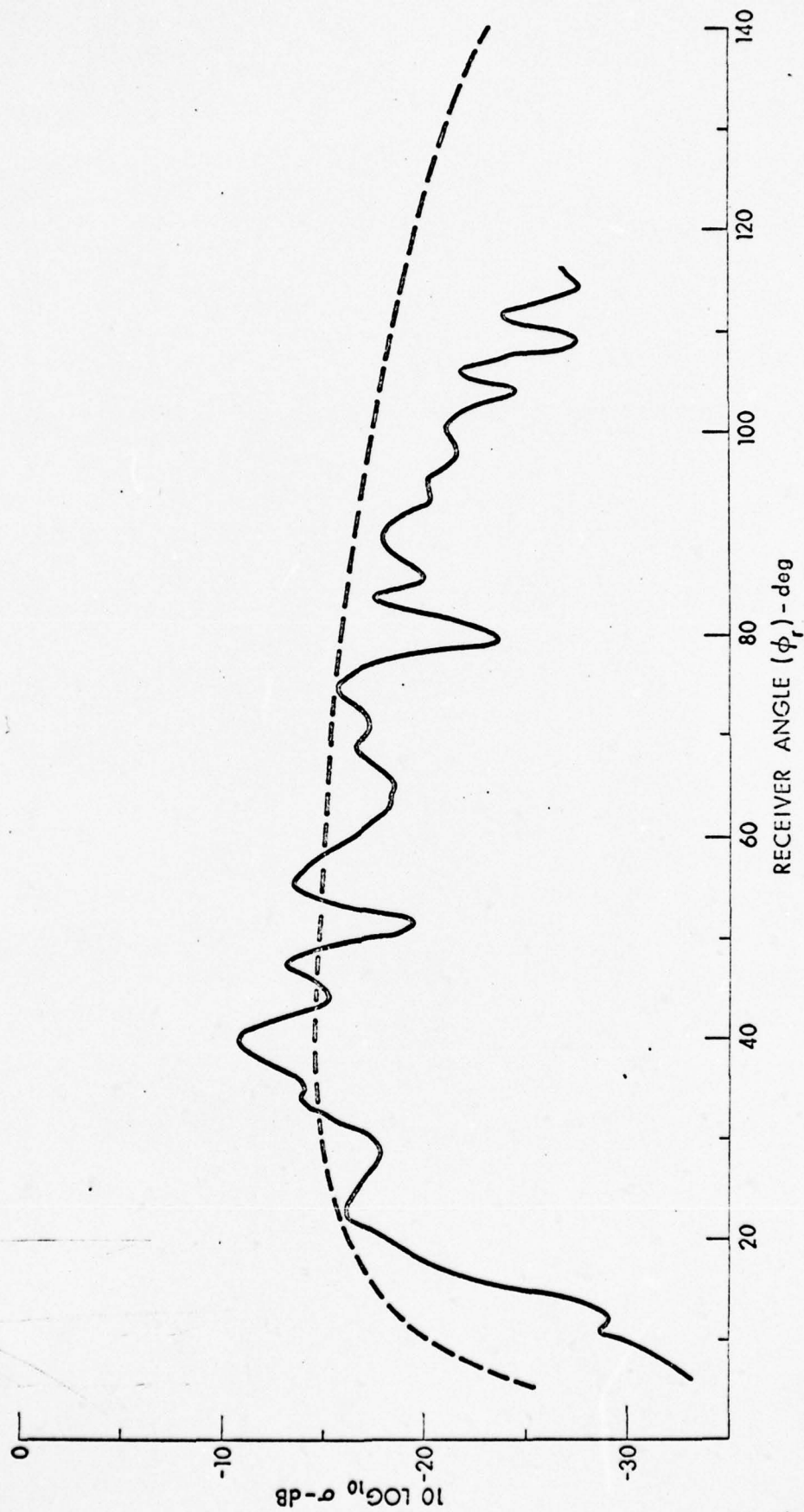
SLIDE 21

BS-66-989
skm 9-11-66



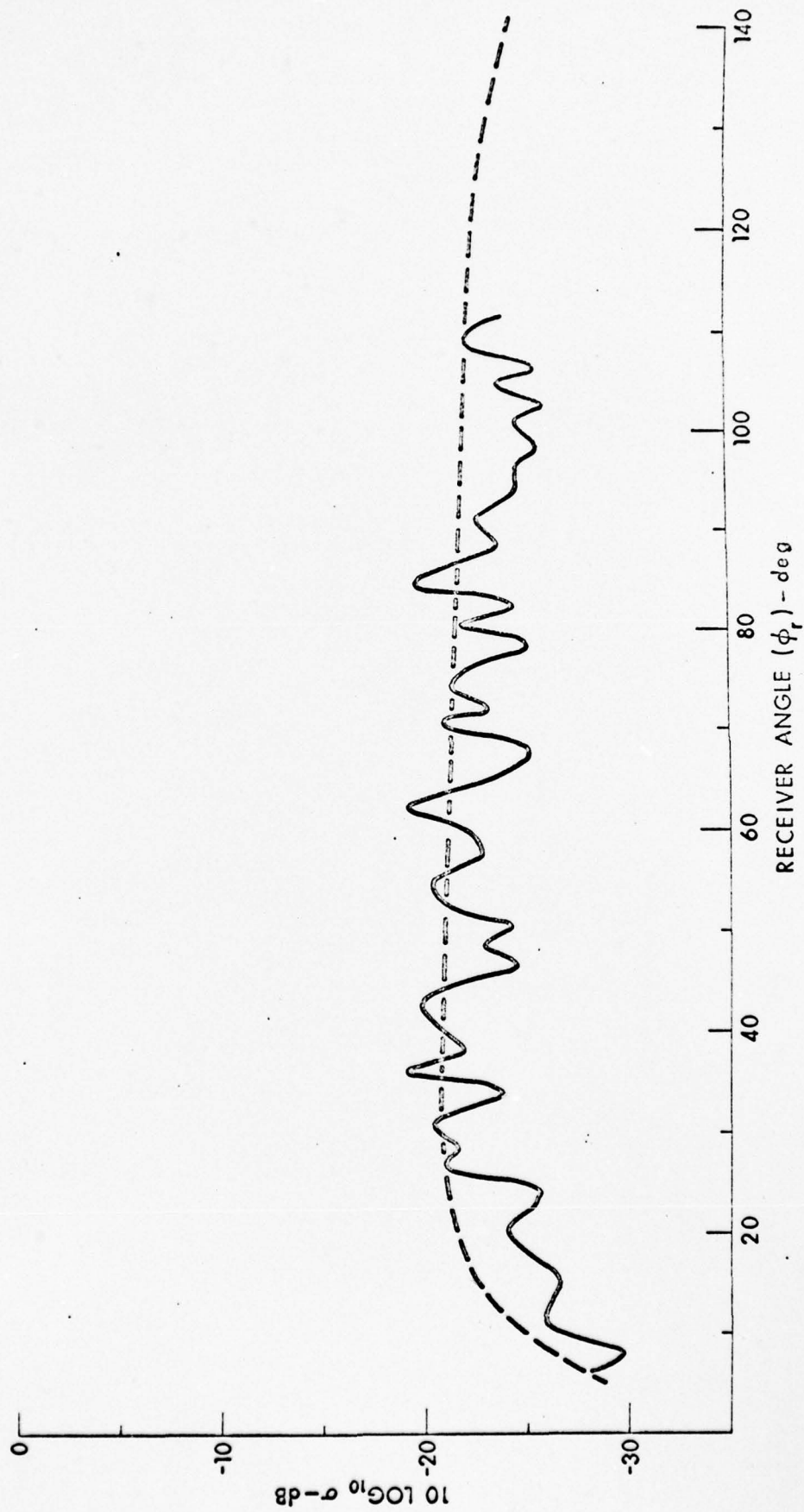
BS-66-940
5KM 9-14-66

SLIDE 22



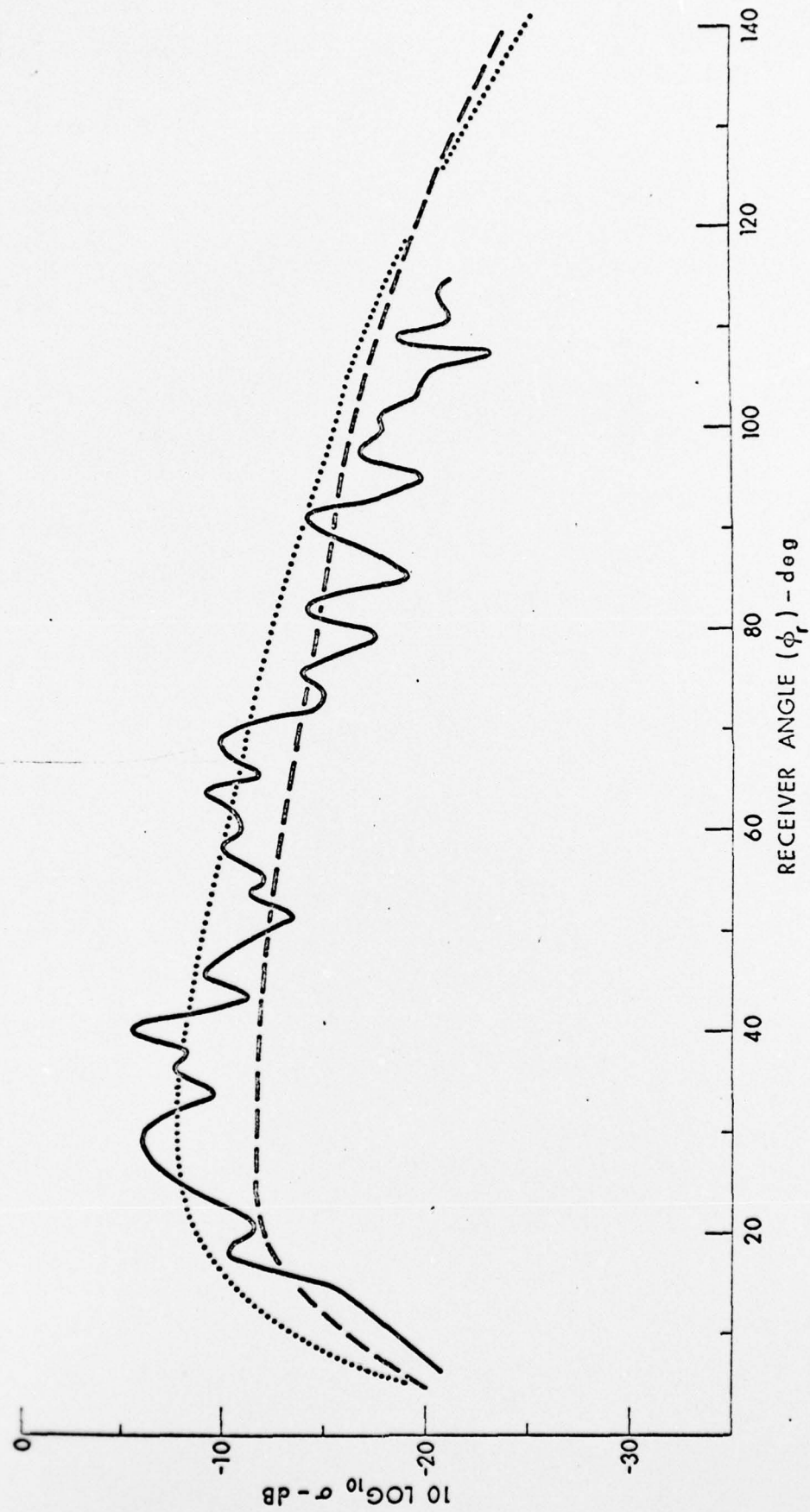
SLIDE 23

BS - 66 - 991
SKM 9-15-66



SLIDE 24

BS-66-942
SKM-7-15-66



SLIDE 25

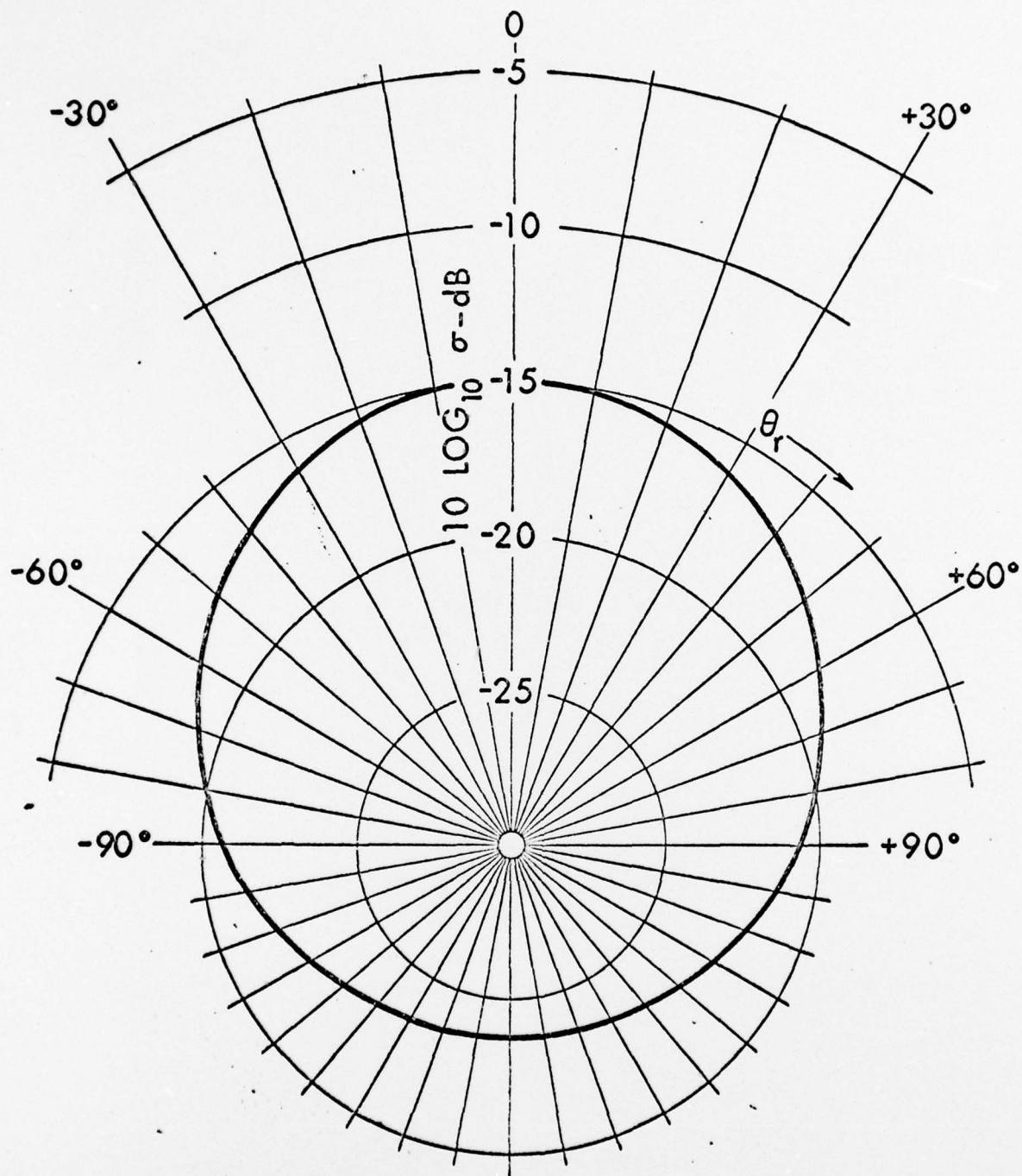
BS-66-943

SKM 9-15-66

relief, and one would expect that the effective value of h^2 , the mean square surface relief, is smaller than the measured value. This argument was used to justify recomputing Eq. 9 with an effective root-mean-square height of $0.8(h^2)$, the value determined from measurements on the model surface. This adjusted curve, which is plotted on this slide with circular dots, agrees well with the observations. This adjustment not only increases the values of σ_m , but it also produces an improvement in the shape of the curve.

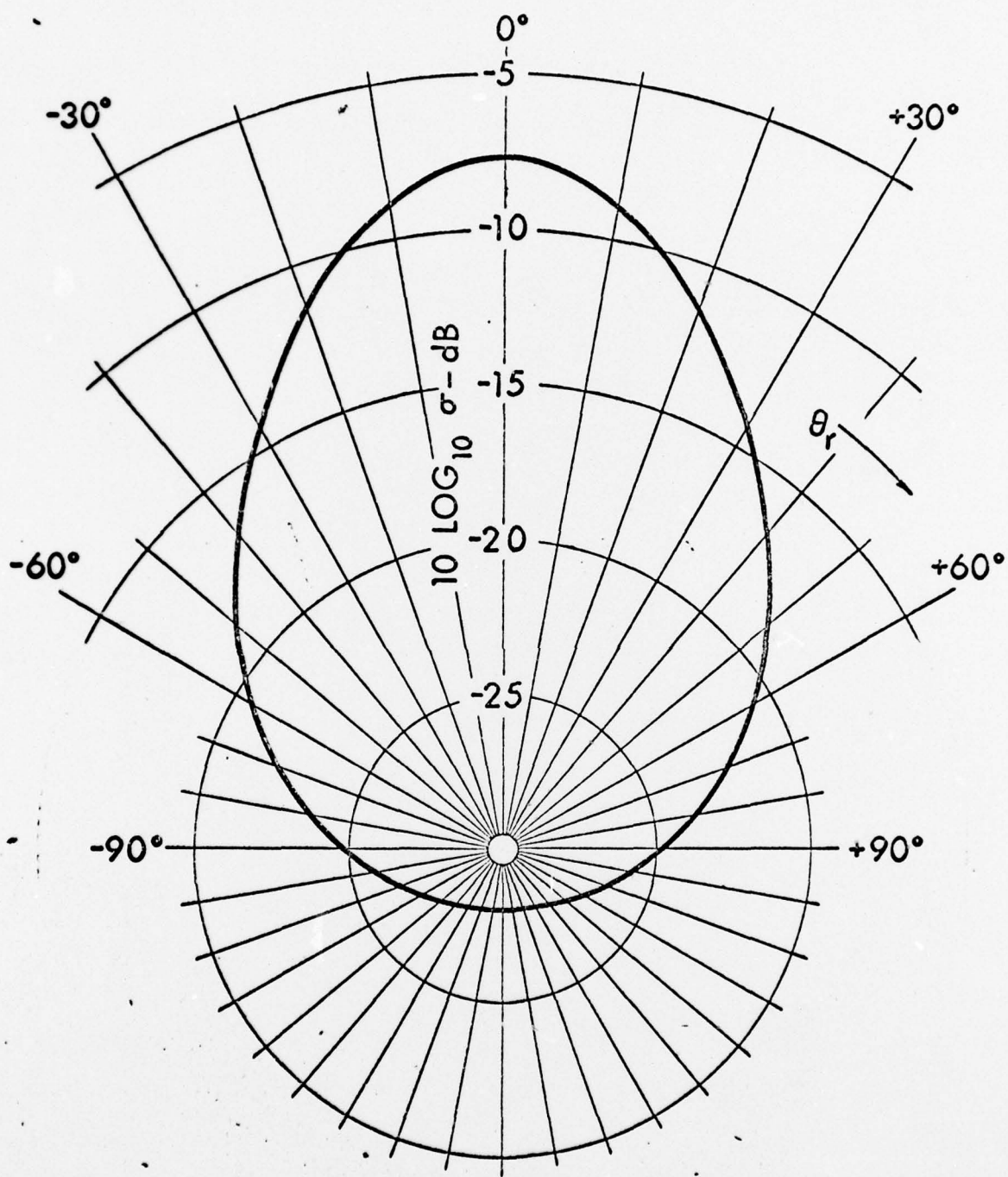
In view of the close agreement between the theoretical and experimental curves seen in the last several slides, one has confidence in the predictions made from Eq. 10 for other scattering angles. SLIDE 26 contains a polar plot of $\sigma_M(\phi_i, \phi_r, \theta_r)$ versus θ_r for $\phi_i = \phi_r = 40$ deg, $f = 100$ kHz, and the model surface relief. SLIDE 27 is a similar plot of σ_M versus θ_r for $\phi_i = \phi_r = 30$ deg. The effective value of $0.8(h^2)$ for the surface relief was used in this calculation in accordance with the agreement given above. These curves show clearly how the roughness of the surface broadens the scattered radiation pattern in the θ_r -direction, and one can see how, as the grazing angle becomes smaller, the scattered energy is removed from the backward and sideward direction and concentrated in the forward direction.

Experimental measurements of the scattering coefficient as a function of incident angle have been made for three other random surfaces. The experimental procedures used for these surfaces were similar to those used for the first surface. The surface described previously will be referred to hereafter as SURFACE I. One of the other surfaces, SURFACE III, is similar to SURFACE I with the exception that the relief has been compressed by a factor of one-half with respect to SURFACE I. SURFACE IV is also similar to SURFACE I except its



SLIDE 36

DRL - UT
DWG AS-66-944
SKM - RFO
9 - 20 - 66



SLIDE 27

DRL - UT
 DWG AS-66-945
 SKM - RFO
 9 - 20 - 66

7 March 1967

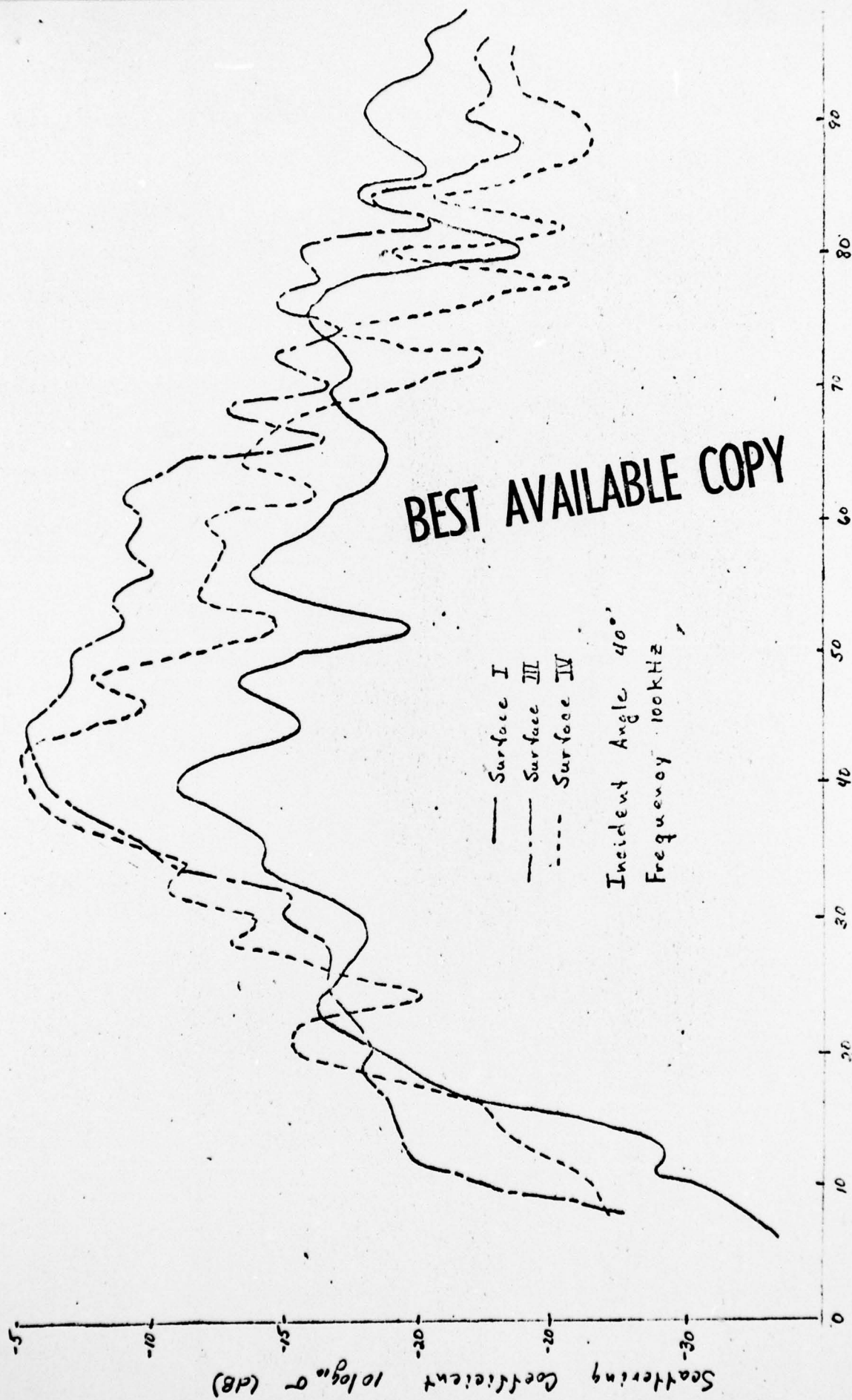
GRB:sv

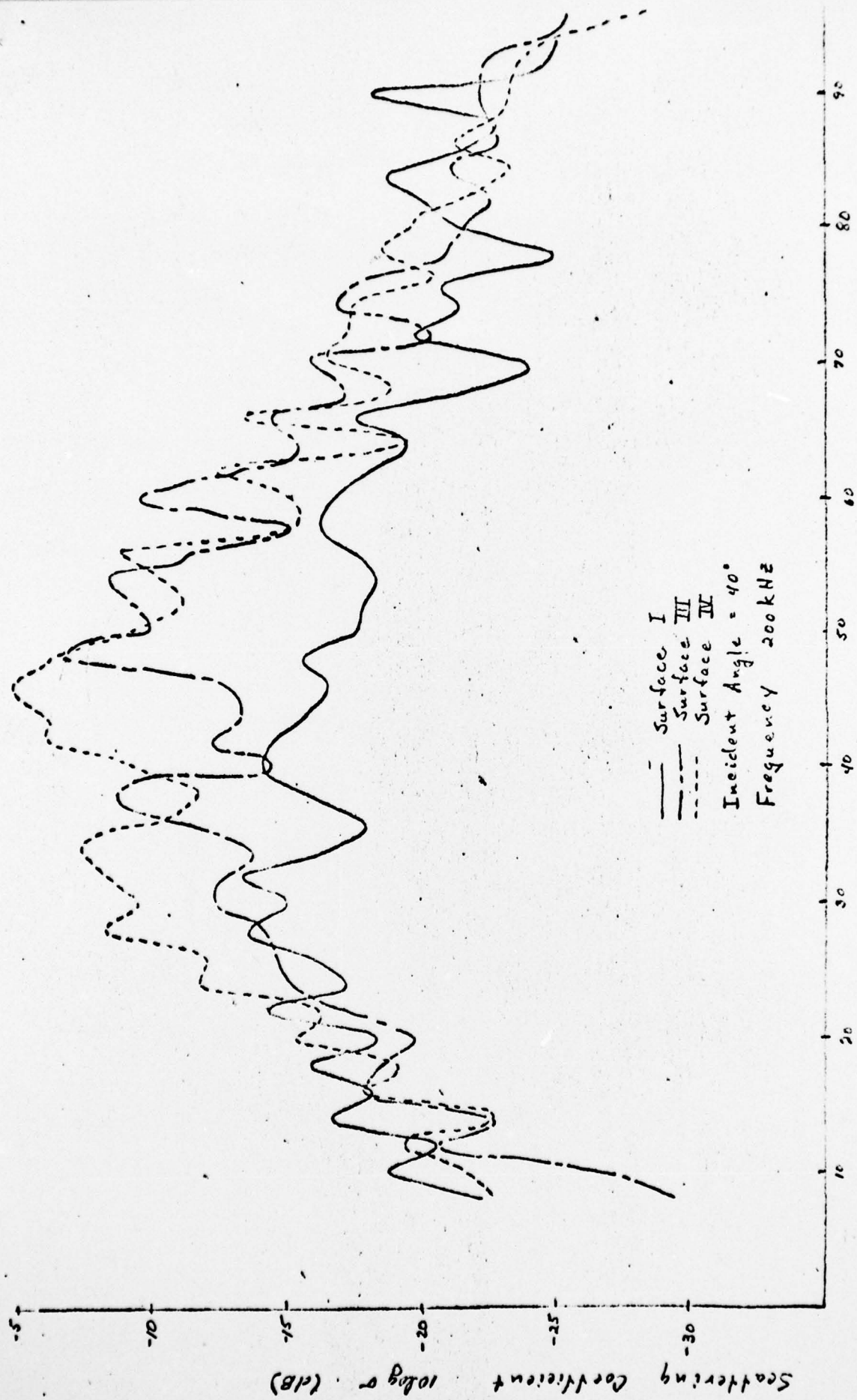
Page 15

relief has been compressed by a factor of one-fourth with respect to SURFACE I. SURFACE II has approximately the same root-mean-square height as SURFACE I and represents one-fourth of SURFACE I expanded in horizontal dimensions by a factor of two. The high frequency case as presented by Eckart and modified as described previously appears to be adequate for SURFACE I when signals of 100 kHz and 200 kHz are used. For SURFACE II, which has the same anomaly height to wavelength ratio as SURFACE I, it is expected that the high frequency limit will still be applicable. For SURFACE II and especially SURFACE III which have root-mean-square heights of 0.38 cm and 0.22 cm, the applicability of the high frequency limit is questionable. No comparisons of the high frequency limit or modifications of this limiting case and the experimental measurements have been made at this time.

SLIDE 28 is a composite of the experimentally measured scattering coefficients for SURFACES I, III, and IV for an incident angle of 40 deg and a frequency of 100 kHz. In the specular direction, it is certain that the scattering coefficient for SURFACE I, the surface with the maximum relief of the three surfaces, is below that of the other two surfaces. However, from this preliminary data, no definite statement can be made on the difference between the scattering coefficients for SURFACE III and SURFACE IV. SLIDE 29 illustrates data similar to that shown in SLIDE 28 with the exception that the frequency is 200 kHz. Again the scattering in the specular direction for SURFACE I is below that of the other two surfaces, and it appears that the specular scattering from SURFACE III is slightly below that from SURFACE IV. This result might be expected, since as the surface becomes smoother more energy would be scattered in the specular direction.

A comparison of the absolute scattering coefficients in the specular





SLIDE 29

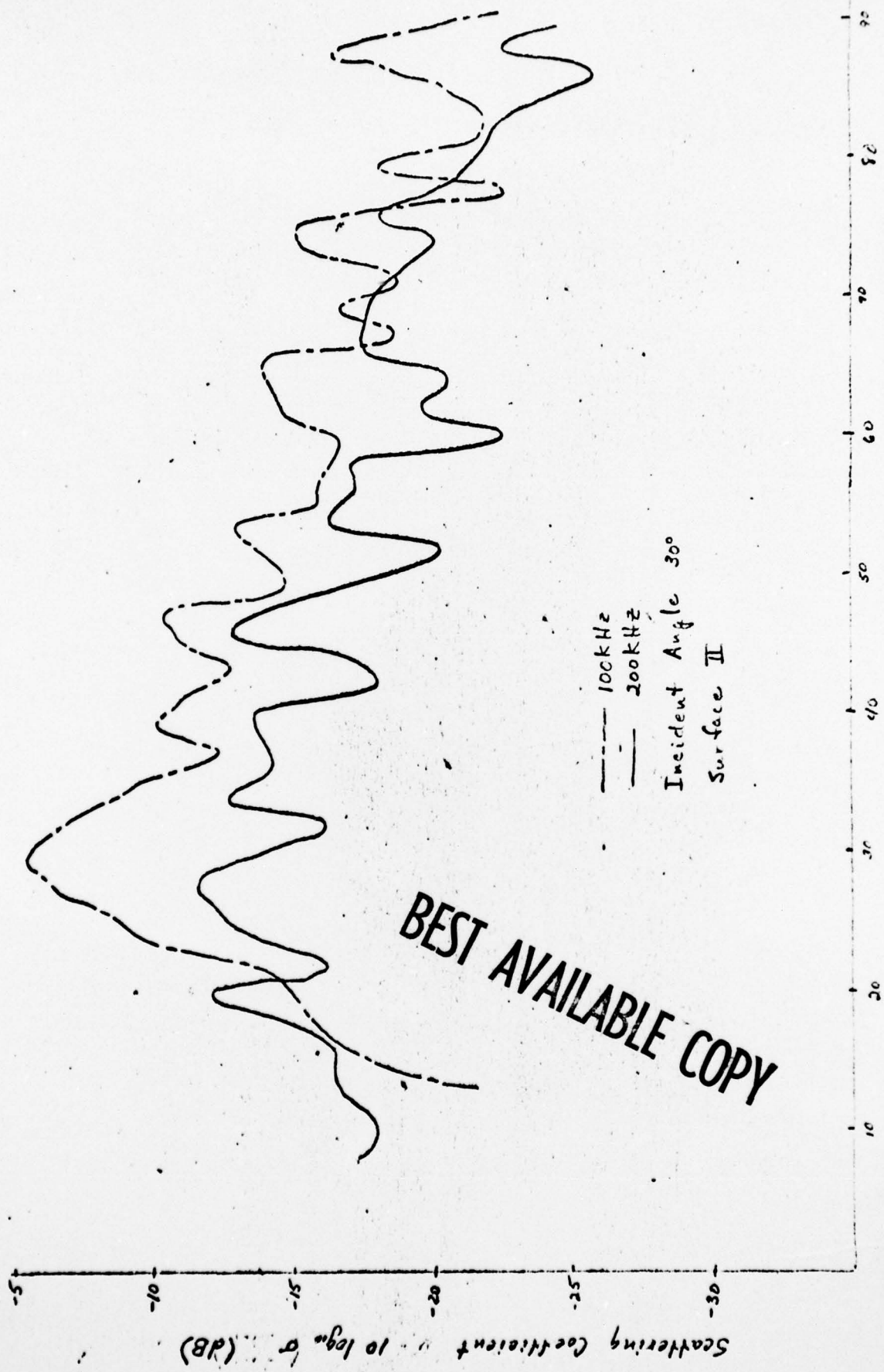
SLIDE 29

direction for the three surfaces at 100 kHz and 200 kHz indicates little, if any, variation with frequency.

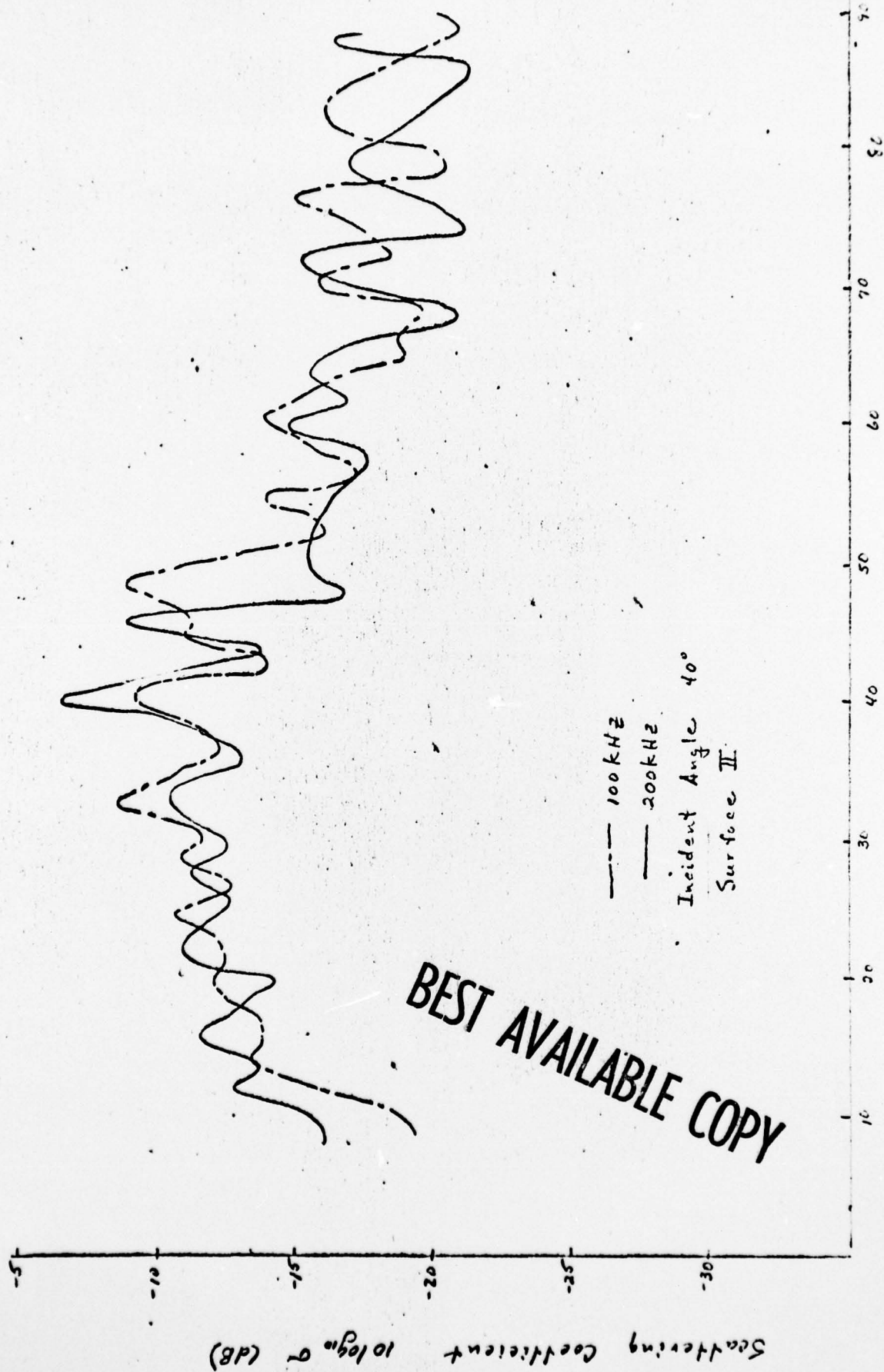
SLIDE 30 illustrates the measured scattering coefficient for SURFACE II, the horizontally expanded version of SURFACE I, for an incident angle of 30 deg and for frequencies of 100 kHz and 200 kHz. These curves appear to indicate a definite frequency dependence. SLIDE 31, however, does not appear to indicate any frequency dependence when the incident angle is 40 deg. Further analysis of the data may or may not substantiate this apparent frequency dependence with incident angle as illustrated by this and the previous slide. An inspection of the data indicates no such frequency dependence upon incident angle for the other surfaces.

SLIDE 32 illustrates the comparison of measured scattering coefficients at 100 kHz and for an incident angle of 40 deg for SURFACE I and for SURFACE II. For receiver angles greater than 30 deg, these measured values are approximately equal. Theoretically, in the high frequency case, it would be expected that the scattering coefficient for SURFACE II would be greater than that for SURFACE I.

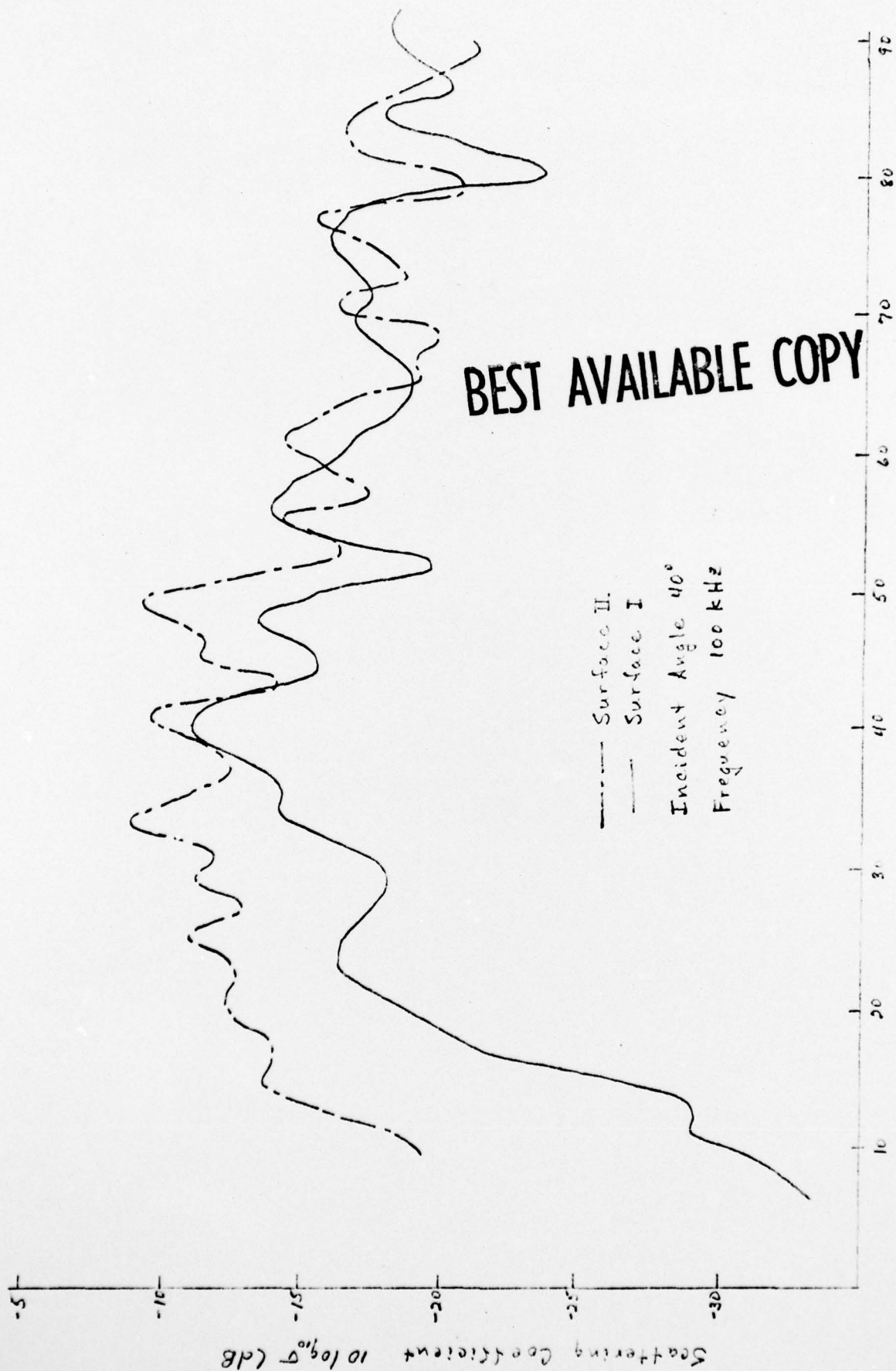
SLIDE 33 illustrates a comparison of the scattering coefficient at 200 kHz for SURFACE I and at 100 kHz for SURFACE III. These two situations involve approximately equal anomaly height to wavelength ratios. For the high frequency case, it would be expected that the scattering coefficient in the specular direction for SURFACE III at 200 kHz would be about 6 dB greater than the specular scattering coefficient for SURFACE I at 100 kHz. As is evident from this slide, the general trend for SURFACE III is somewhat greater than for SURFACE I.

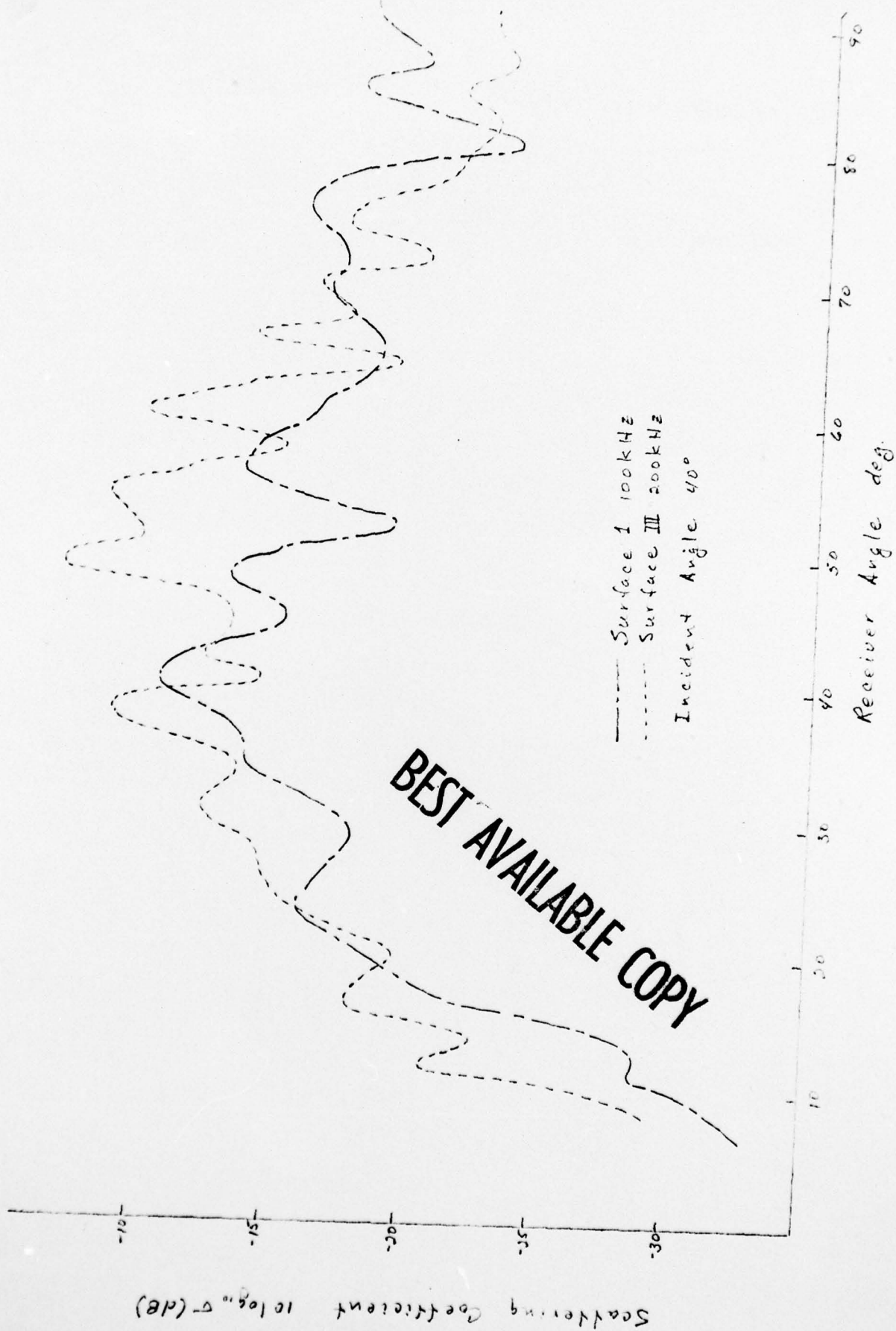


BEST AVAILABLE COPY



BEST AVAILABLE COPY





Conclusions

Experimentally measured scattering coefficients as a function of incident angle and frequency for the rough surface, SURFACE I, are in substantial agreement with predicted values using a modified version of the short wavelength limit scattering formula developed by Eckart. The modifications to this theory are related to the specification of a boundary condition on the surface and to the technique of assuming root-mean-square surface heights less than measured values to account for shadowing of portions of the scattering surface at low grazing angles.

From the preliminary data available to date for the scattering coefficient as a function of incident angle and frequency for SURFACES II, III, and IV, no definite statements can be made concerning comparisons with theoretically predicted values. At this time, only general trends and relative values of the scattering coefficient in the specular direction can be compared. Both the high and low frequency cases of Eckart's theory will be studied and possibly modified further with subsequent comparisons with measurements.

7 March 1967

GRB:sv

Page 18

References

1. G. R. Barnard, J. L. Bardin, and W. B. Hemphkins, J. Acoust. Soc. Am. 36, 2119-2123 (1964).
2. J. L. Uretsky, Ann. Phys. 33, 400-427 (1965).
3. G. R. Barnard, C. W. Horton, M. K. Miller, F. R. Spitznogle, J. Acoust. Soc. Am. 39, 1162-1169 (1966).
4. C. W. Horton, W. B. Hemkins, A. A. J. Hoffman, Geophysics 29, 582-601 (1964).
5. P. Beckmann and A. Spizzichino, The Scattering of Electromagnetic Waves from Rough Surfaces, (Pergamon Press, London, 1963)
6. C. Eckart, J. Acoust. Soc. Am. 25, 566-570 (1953).
7. C. W. Horton and G. S. Innis, Jr., J. Acoust. Soc. Am. 33, 877-880 (1961).
8. D. D. Baker, J. Acoust. Soc. Am. 34, 1737-1744 (1962).
9. C. W. Horton and T. G. Muir (To be published in March, 1967, issue of J. Acoust. Soc. Am.)
10. C. W. Horton, S. K. Mitchell, and G. R. Barnard (To be published in March, 1967, issue of J. Acoust. Soc. Am.)